THREE DIMENSIONAL ELECTRODE INTEGRATION ON MICROWAVE RESONATOR SENSORS FOR MICROPARTICLE SENSING IN MICROFLUIDICS

A THESIS SUBMITTED TO

THE GRADUATE SCHOOL OF ENGINEERING AND SCIENCE

OF BILKENT UNIVERSITY

IN PARTIAL FULFILLMENT OF THE REQUIREMENTS FOR

THE DEGREE OF

MASTER OF SCIENCE

IN

MECHANICAL ENGINEERING

By

Yağmur Ceren Alataş

June 2024

Three Dimensional Electrode Integration on Microwave Resonator Sensors for Microparticle Sensing in Microfluidics
By Yağmur Ceren Alataş
June 2024

We certify that we have read this thesis and that in our opinion it is fully adequate, in scope and in quality, as a thesis for the degree of Master of Science.

Mehmet Selim Hanay(Advisor)

Gökberk Kabacaoğlu

Abdulsalam Aji Suleiman

Approved for the Graduate School of Engineering and Science:

Orhan Arıkan
Director of the Graduate School

ABSTRACT

THREE DIMENSIONAL ELECTRODE INTEGRATION ON MICROWAVE RESONATOR SENSORS FOR MICROPARTICLE SENSING IN MICROFLUIDICS

Yağmur Ceren Alataş
M.S. in Mechanical Engineering
Advisor: Mehmet Selim Hanay
June 2024

Position dependency of the particle-induced signal can be mitigated by using a 3-dimensional (3D) electrode configuration at the sidewalls of the microfluidic channel in electrical sensors. The first method to obtain 3D electrodes was filling Galinstan, Galium-Indium alloy with low melting point, to dead-end PDMS cavities at the sidewalls of a microfluidic channel positioned on a split ring resonator (SRR). Due to electrical contact between coplanar resonator electrodes and Galinstan cavities, the electric field between coplanar resonator electrodes was extended to form a uniform electric field along the height of the microfluidic channel. Galinstan was used in this application due to its low melting point, non-toxicity, and high conductivity. This architecture was used for size-based classification of 20-and 30µm polystyrene (PS) microparticles without any post-processing for particle trajectory. However, the signal-to-noise ratio (SNR) was low due to the presence of PDMS spacers between the Galinstan cavities and the microfluidic channel, which were placed to avoid leakage of liquid metal into the microfluidic channel.

In the later method, 3D electrodes made of solid material, epoxy-based, negative photoresist SU8, were fabricated and positioned inside a microfluidic channel to boost the signal-to-noise ratio. SU8 pillars with tens of micrometers height were patterned at the sensing region and metalized using sputter deposition to form a conformal profile on the electrodes. A fused silica substrate containing the SU8 microelectrodes, microfluidic channel, and coplanar connection electrodes was mounted on a microstrip transmission line resonator on PCB. The electric field on the resonator electrodes was extended to form a uniform electric field inside the microfluidic channel between the SU8 microelectrodes through wire-bonding on connection electrodes. This sensor architecture was also used for

size-based classification of 12-and 20µm polystyrene microparticles without any trajectory correction. As a result of positioning 3D electrodes in direct contact with the microfluidic channel, the signal-to-noise ratio increased by 10 folds.

Furthermore, a split ring resonator was integrated with a Coulter counter operating at low frequencies to measure the size and dielectric permittivity of a microparticle simultaneously. SU8 microelectrodes were fabricated at the tip of low and high-frequency sensing electrodes, positioned inside the microfluidic channel, forming the sensing region. The signals induced in the split ring resonator and Coulter counter can be simultaneously processed to get information about the size and type of the particle. Polystyrene and polyethylene microparticles with different dielectric permittivity and size were differentiated with this sensor. It was realized that polyethylene microparticles contained additives, which were not explicitly stated, however, the presence of titanium dioxide was detected using energy-dispersive X-ray spectroscopy (EDX). It was concluded that as a result of using a microwave resonator, it was possible to detect the presence of titanium dioxide inside the polyethylene microparticles and differentiate polystyrene and polyethylene particles.

Keywords: Capacitative sensing, microwave, resonator, microfluidics, 3 dimensional microelectrodes, microparticle sensing.

ÖZET

MIKROPARÇACK ALGLAMA IÇIN MIKROAKSKAN-MIKRODALGA SENSÖRLER ÜZERINE 3 BOYUTLU ELEKTROT ENTEGRASYONU

Yağmur Ceren Alataş
Makine Mühendisliği, Yüksek Lisans
Tez Danışmanı: Mehmet Selim Hanay
Haziran 2024

Elektronik sensörlerde parçacık tarafından oluşturulan sinyalin parçacığın kanaldaki yüksekliğinden bağımsız olmasını sağlamak için mikroakışkan kanal duvarlarında 3 boyutlu elektrotlar kullanılabilir. 3-boyutlu elektrot oluşturmak için ilk metot olarak mikroakışkan kanalın duvarlarında bulunan PDMS kanallara oda sıcaklığında sıvı halde bulunan Galinstan materyali enjekte edilmiştir. Galinstan kanalları, bölünmüş halka rezonatörünün ince elektrotları üzerine konumlandırılmıştır. Galinstan kanalları ve rezonatörün ince elektrotları arasındaki elektriksel bağlantı sayesinde rezonatör üzerinde oluşan elektrik alan mikroakışkan kanal içesinde sabit elektrik alan oluşması için uzatılabilmiştir. Galinstan materyali, düşük erime sıcaklığı, insanlar için zararsız olması ve yüksek iletkenliği sebebiyle sensörde kullanılmıştır. Bu sensör kullanılarak 20 ve 30 mikrometre boyutlarındaki polistren parçacıklar boyutlarına göre ayrıştırılabilmiştir. 3 boyutlu elektrot yapısı kullanıldığı için parçacığın kanaldaki yüksekliğini bulmak için sinyal işleme yapılmamıştır. Sıvı metalin mikroakışkan kanala sızmasını engellemek için konulan PDMS duvarlar, sensörün sinyal-gürültü oranının düşmesine yol açmıştır.

Daha sonra, 3 boyutlu elektrot üretmek için eposki bazlı negatif bir fotorezist olan SU8 materyali kullanılmış ve 3 boyutlu elektrotlar katı bir maddeden yapıldığı için mikroakışkan kanal içerisine konulabilmiştir. Bu şekilde sensörün sinyal-gürültü oranı arttırılabilmiştir. Mikrometre kalınlığındaki SU8 prizmalar sensörün algılama bölgesinde üretilmiş ve püskürtme tekniği ile prizmanın iç duvarları kaplanabilmiştir. SU8 elektrotlar, mikroakışkan kanal ve bağlantı elektrotlarını bulunduran silika substrat, PCB üzerinde bulundan mikrodalga rezonatöre bağlanmıştır. Rezonatör üzerinde oluşturulan elektrik alan, bağlantı elektrotları

üzerinden tel bağlama tekniği ile SU8 prizmalara iletilmiş bu şekilde mikrokanal içerisine sabit elektrik alan oluşturulabilmiştir. Bu sensör yapısı, 12 ve 20 mikrometre polistrien parçacıkların boyuta göre ayrıştırılması için kullanılmıştır. Bu şekilde parçacığın kanal içerisindeki yüksekliğini bulmak için sinyal işleme yapılmasına gerek duyulmamıştır. 3 boyutlu elektrolar kanaldan geçen sıvı ile direkt temas ettiği için sinyal-gürültü oranı 10 katına kadar arttırılabilmiştir.

Daha sonra, bölünmüş halka rezonatörü Coulter sayacı ile birleştirilmiş, bu şekilde hem boyut hem de dielektrik geçirgenlik ölçümü yapılmıştır. SU8 mikroelektrotlar yüksek ve alçak frekansta çalışan sensörlerin üzerine, algılama bölgesi oluşturulacak şekilde üretilmiştir. Rezonatör ve Coulter sayacı sinyalleri birlikte analiz edilerek parçacığın hem boyutu hem de dielektrik geçirgenliği ölçülmüştür. Bu yapı kullanılarak farklı boyut ve geçirgenlikteki polistren ve polietilen parçacıklar ayrıştırılmıştır. EDX ölçümü sonrasında polietilen parçacıkların içerisinde titanyum dioksit başta olmak üzere başka bileşlenlerin bulunduğu ve bu yüzden parçacığın dielektrik geçirgenliğinin değiştiği sonucu çıkarılmıştır. Deney sonuçları görüldüğünde, mikrodalga rezonatör kullanılarak parçacığın içindeki titanyum dioksitin etkisinin ölçüldüğü görülmüştür.

Anahtar sözcükler: Kapasitatif algılama, mikrodalga, rezonatör, mikroakışkanlar, 3 boyutlu mikroelektrotlar, mikroparçacık algılama.

Acknowledgement

First of all, I would like to thank my advisor, Dr. Mehnet Selim Hanay, who has given me the opportunity to be a part of his research group, starting from the early years of my undergraduate. He has always been the most patient, intelligent and calm PI one can ever imagine. Without his feedback and insights these works wouldn't have been realized. Thanks to my jury members, Dr. Abdulsalam Aji Suleiman and Dr. Gökberk Kabacaoğlu for their time, understanding and valuable feedbacks. I also want to thank Dr. Yegan Erdem and Dr. Fatih Inci for their inspiring courses and guidance.

I want to thank current members and alumni of Hanay Group: Sayedus Salehin, Batuhan Emre Kaynak, Mohammed Alkhaled, Uzay Tefek, Chullhyeong Lee, Berk Küçükoğlu, Burak Sarı, Enise Kartal for their friendship and help in the projects. Sincere thanks to Murat Güre and Kadir Ulak for their help in microfabrication and wirebonding.

I am grateful for my best friend, Taha Ilıkkan, who supported me continuously and showed me how to have fun even during stressful times. I will truly miss dancing in the cleanroom, and making fun of people with you. I am also thankful to my friends; Yusuf Aslan, Koray Yavuz, Sare Nur Çuhadar, Erim Uzunoğlu, Ece Karabey, Ahsan Tauseef, and Amirali Aleali for their friendship and support. I also want to thank my lifelong friends; Hazal Aksu, Emre Özalp, Emre Polat, Ece Kayacılar, and Orkan Oztrak. I am most grateful for my best friends; Birce Nur Altunsu and Çınar Gülleroğlu (a.k.a Çınçın) for being the funniest, most sincere people in my life. Even the smallest conversation with you always makes my day better.

Most importantly, I would like to thank my family for always being there for me, supporting and guiding me at every step. There are no words to express how thankful I am, I love you.

Contents

List of Figures

List of Tables

Chapter 1

Introduction

Microfluidics-integrated electrical sensors can be used for label-free characterization of microparticles and cells with high throughput and single particle level accuracy. When an analyte microparticle passes through the sensing region of the sensor, it modifies the electric field distribution between the electrodes, causing a shift in the sensor's impedance. For electronic sensors operating at low frequencies, the conductivity of the solute ions has an important role. For example, an ionic current is created in resistive pulse sensing due to the solute ions acting as charge carriers. When a dielectric particle passes between the electrodes, it causes a decrease in ionic current proportional to its size [1]. Resistive pulse sensing has various applications in the literature such as counting and detecting cells, viruses, and extracellular vesicles (EVs) [2], DNA sequencing in nanopore devices [3].

Another emerging approach is to use capacitative sensors that operate at higher frequencies e.g. at microwave band [4] [5] [6] [7] [8] [9] [10] [11] [12] [13], where the ion motion can not follow the electric field therefore ionic current is bypassed. Microparticles induce a capacitance shift in the sensor proportional to the square of the electric field magnitude between the electrodes, which can be measured with high accuracy using resonance-based detection. Capacitance shift translates as a shift in resonance frequency or phase and amplitude of the resonator and it can be

measured by phase-sensitive detection [8] [14] [15]. An advantage associated with capacitative sensing is that the signal contains information about the dielectric permittivity of the analyte microparticle in addition to its size, which can be useful for distinguishing microparticles based on dielectric permittivity [16]

Electrodes can be configured in three ways in microfluidics integrated electrical sensors: coplanar, parallel-plate structure with electrodes at the top and bottom of the microfluidic channel, or 3D electrodes at the sidewalls of the microfluidic channel. Among these configurations, the fabrication of coplanar electrodes is simple yet the electric field magnitude is non-uniform; the magnitude of the electric field decreases with the distance from the electrodes along the height of the microfluidic channel. Due to this non-uniformity, the signal induced by a particle depends on its trajectory inside the microfluidic channel causing positional dependency. There are several approaches to tackle positional dependency in coplanar electrodes: The same microparticle can be measured with multiple electrodes operating at RF [17] [18] [19]or microwave band [16] or microparticles can be focused to a single trajectory using either inertial [20], sheath flow [21] or viscoelastic focusing [22] approaches.

Another alternative to mitigate positional dependency is to use either parallel plate or 3D electrode configurations to create a uniform electric field inside the microfluidic channel. Yet, these configurations require more steps in metallization or wafer bonding. For parallel-plate electrode configuration, coplanar electrodes can be patterned on two separate substrates by photolithography and thermal evaporation, later these substrates are bonded using thermal, vacuum, or adhesive bonding procedures. An example of thermal bonding is the work of Mc. Grath et. al. where they fabricated an impedance cytometer with parallel plate electrode configuration through bonding the substrates under high temperature and pressure after patterning the coplanar electrodes. The impedance cytometer was used to conduct electrophysiological measurements on pancreatic cancer cells [23]. For adhesive bonding, surface-treated SU8 can be used both to define microfluidic channels and to bond either silicon-glass or glass-glass substrates [24]. An example of using SU8 for adhesive bonding is the work of Haandbæk et. al. where they built an impedance cytometer integrated with a resonator for the

detection of sub-micrometer particles. SU8 was used to define the microfluidic channel and bond the glass substrates with coplanar electrodes [25]. UV curable adhesive can also be used to bond substrates, Han& Han fabricated a microfluidic device for the enrichment and electrical detection of circulating tumor cells (CTCs). Substrates with coplanar electrodes were bonded by the application of a UV-curable adhesive [26]. Vacuum bonding was used by Spencer & Morgan (2020) where they bonded glass substrates with coplanar electrodes in a vacuum bonder to fabricate an impedance cytometer for analysis of the dielectric properties of single cells by bonding the [19]. Although these bonding methods provide good sealing between the substrates, there are several disadvantages associated with each: High temperature and pressure might deform the microfluidic channels and damage the metal layers in the chip for thermal and vacuum bonding techniques. Adhesive bonding can be applied to any material however extensive surface cleaning is necessary before the bonding.

The last alternative to obtain a uniform electric field inside the microfluidic channel is positioning 3D electrodes made of either a solid material or filled with a liquid to the sidewalls of the microfluidic channel. For solid electrodes, the fabrication of electrodes with tens of micrometers thickness, which requires the use of non-standard metalization processes, requires more steps compared to previously described electrode configurations. Examples of 3D electrodes in the literature are explained in further detail in the below subsections.

In this thesis, 3D electrodes made of solid material and filled with liquid metal were fabricated on Microfluidics-Integrated Microwave Sensors (MIMS) to mitigate the positional dependency in microwave sensors. 3D electrodes were positioned at the sensing region of the underlying coplanar microwave resonator sensor and the electric field on the coplanar structure was extended to form a uniform electric field inside the microfluidic channel due to the contact between 3D and coplanar structures. Cleanroom patterning and deposition techniques were used to fabricate the 3D electrodes. Initially, 3D electrode integrated microwave resonator architecture was used for size-based classification between polystyrene microparticles. After adding a low-frequency sensor to the architecture, additional experiments were conducted to distinguish microparticles based on size

and dielectric permittivity.

1.1 Liquid Electrodes

Liquid-filled 3D electrodes are obtained by filling a conductive solution into the dead-end access channels located at the sidewalls of the microfluidic channel. The conductive solution in these channels is electrically accessed by thin metal electrodes deposited at the bottom of the channel. The voltage is applied to the coplanar electrodes and transmitted to the conductive solution inside the access channel: As a result, the boundary between the access channel and the microfluidic channel becomes an equipotential surface, creating a uniform electric field along the height of the microfluidic channel. Conductive salt solutions can be used for applications operating at low frequencies (MHz range) where ion motion can follow the applied frequency [27].

Liquid electrodes were used in various microfluidics applications: Rao et.al. injected silver paste inside electrode channels and used this architecture for droplet and cell sorting applications [28]. McIntyre et.al. filled conductive ink inside thermoplastic microfluidic chips and demonstrated the use of the resultant chip for capacitance sensing, droplet merging, and droplet sorting [29]. Puttaswamy et. al. used a composite liquid electrode made of conductive carbon powder and adhesive and demonstrated DEP particle switching [30]. Furthermore, Sciambi & Abate built a microfluidic chip for droplet manipulation applications in which electrodes were obtained by filling salt water into guide channels [31]. Tang et. al. obtained 3D electrodes by dipping Ag/AgCl wires into electrode channels filled with highly conductive KCl solution for microfluidic impedance cytometry for counting and differentiating cells [32]. Moreover, several ionic liquids e.g. 1-butyl-3-methyl-imidazolium tetrafluoroborate were used as liquid electrodes in capacitative sensing and microfluidics applications [33] [34].

The conductive solutions used to obtain the 3D electrodes in the aforementioned studies are not applicable for use at high frequencies e.g. microwave band,

due to the decrease in the ion mobility. Instead, metals with low melting point are more suitable because of their high conductivity. There are a few examples of using metals with low melting point in microfluidic applications in the literature. For instance, Bismuth alloy microspheres (melting point: 46.5 °C) were placed near the sidewalls of the microfluidic channel and the device was heated so that Bismuth melted and filled the electrode gaps. The device was used for DEP applications [35].

Furthermore, Galinstan (Eutectic Galium Indium alloy) is commonly used in microfluidics due to its low melting point (15.7 °C), high conductivity, and being non-toxic for humans. Due to its low melting point, Galinstan is liquid at room temperature so, it can be injected inside electrode cavities in microfluidic systems. Galinstan was used in flexible electronics such as strain sensor [36], energy harvester [37], and stretchable RFID antenna applications [38]. Furthermore, Munirathinam et.al. fabricated a capacitor and inductor inside PDMS by injecting Galinstan to build a capacitative sensor for wireless pressure monitoring [39]. In addition to injection, there are various methods to fabricate Galinstan microstructures inside microfluidic devices. Tang et.al. used DEP to immobilize Galinstan and form electrodes inside the microfluidic channel and demonstrated applications for nanoparticle trapping and as microfins for improving heat dissipation [40]. There are several examples of the use of Galinstan at high frequencies due to its high conductivity: Frequency-tunable microwave resonator structure was developed by controlled placement Galinstan on a microwave resonator [41] [42]. Gao et.al. built a metasurface for controllable electromagnetic wave reflection attenuation using Galinstan-filled split ring resonators [43].

In the first part of this thesis, Galinstan is used to form 3D electrodes at the sidewalls of a microfluidic channel integrated on a split ring resonator (SRR) operating in microwave regime. Galinstan was injected into dead-end access channels at the sidewalls of the microfluidic channel. Size-based classification experiments were conducted using 20 and 30µm polystyrene microparticles to test the 3D electrode integrated resonator architecture.

1.2 Solid 3D Electrodes

Fabrication of solid 3D electrodes on microfluidics sensors requires deposition of metal structures with thickness on the order of tens of micrometers, which can not be achieved by standard cleanroom procedures. As a result, various techniques were developed for 3D electrode fabrication in literature with or without using cleanroom processes. An example of 3D electrode fabrication without using cleanroom is the work of Zeinali et.al. where they fabricated 3D electrodes with thickness around by mechanical micromachining (with heights typically $\sim$ 100 µm) for DEP applications. This method yields reusable electrodes with thickness down to around 20µm however, electrodes need to be manually placed at the sidewalls of the microfluidic channel. [44].Furthermore, Güler et.al. placed gold microwires inside the microfluidic channel and formed 3D electrodes by etching the wires for a microparticle counting chip [45]. Nery et.al. used pencil leads as 3D electrodes inside an electrochemical microfluidic system to determine dopamine concentration in physiological pH [46]. Electrospray ionization was also reported as a method to deposit metal, semiconductor, and dielectric materials on surfaces coated with photoresist [47], it can even be used for deposition on active sensor surfaces combined with electrostatic focusing [48]. Methods like inkjet writing, direct ink writing, and aerosol jet 3D printing were used to deposit thick, conductive electrodes for droplet manipulation, DEP, and defining microwave circuits [49] [50] [51].

In the cleanroom, electroplating can be used to deposit metal electrodes at the sidewalls of a microfluidic channel for microfluidic applications like magnetohydrodynamics, DEP, and impedance cytometry [52] [53]. Civelekoglu et.al. fabricated blanket electrodes through sputtering gold at the sidewalls of a PDMS microfluidic channel to obtain a uniform electric field [54]. 3D electrodes can also be obtained by modifying the BiCMOS process or using a thick layer of highly doped Silicon as the electrode layer [55][56].

Another method for fabricating 3D electrodes is patterning polymers like PDMS, Durimide, or SU8, commonly used in soft-lithography workflows. Usually,

these polymers are used for microfluidic channel microfabrication but they can also serve as a structural material for the 3D electrodes. One advantage of using these polymers is that structures with height on the order of tens of micrometers can be fabricated by spin-coating and photolithography, however, an additional step is required for metalization of the structure. For instance, Hu et.al. patterned Durimide 7510 structures with 25µm thickness and trapezoidal wall profile at the sidewalls of the microfluidic channel, later the structures were metalized by gold sputtering. The microfluidic chip was used for cell electrofusion and electroporation [57]. PDMS was also used as 3D electrode by forming a PDMS-silver nanoparticle composite for DEP microfluidic chip [58]. Furthermore, SU8 was also made conductive through mixing with silver nanoparticles inside the photoresist [59]. Another approach to fabricate conductive SU8 microstructures is using pyrolysis procedure where SU8 is carbonized under N2 gas flow at high temperatures to obtain carbonized 3D microelectrodes [60]. Furthermore, Kilchemann et.al. fabricated metal-coated SU8 microelectrodes around a microfluidic channel through sputtering metal on SU8 pillars. In this approach, SU8 pillars were metalized by conformally depositing a thin metal layer with thickness even on the order of several nanometers [61]. The 3D electrodes fabricated with this technique were used for DEP, single-cell trapping and recovery, and analyzing the dielectric properties of single cells by electrorotation [62] [63]. Yet, all these applications operate at low frequencies (MHz regime), so the use of polymer base 3D electrodes in microwave regime has not been shown yet.

In Chapter 4, solid 3D electrodes were fabricated by metalizing SU8 pillars positioned at the sidewalls of a microfluidic channel. SU8 pillars were connected to a microstrip transmission line microwave resonator using wirebonding. This resonator architecture was used to classify 20 and 12 µm polystyrene microparticles based on size. Later, high and low-frequency sensors were combined on a single chip, and 3D SU8 microelectrodes were fabricated on both sensors using a similar fabrication procedure. This architecture was used to distinguish between microparticle species.

Chapter 2

Theory of Operation

This section aims to provide background information regarding the working principles of high and low-frequency sensors used in Chapters 3-5. The first subsection explains how microwave sensors can be used for microparticle sensing based on dielectric permittivity and size. The operation principle of the low-frequency sensor, Coulter Counter, is described in the later subsection.

2.1 Microwave Resonator-based Sensing

A microwave resonator is a frequency-selective device that can store and manipulate electrical and magnetic energy at microwave frequencies. Applications of microwave resonators include security, magnetic resonance imaging (MRI), radar systems, and quantum technology [64]. The resonance phenomenon occurs due to standing waves formed on the structure. Localized electric and magnetic fields formed at the resonance frequency can be exploited for sensing purposes.

The microwave resonator sensor can be modeled as an RLC equivalent circuit with the resonance frequency stated in Equation 2.1.

$$f_0 = \frac{1}{2\pi\sqrt{LC}} \tag{2.1}$$

Passage of a microparticle between the electrodes at the sensing region creates an instantaneous shift in the capacitance of the system which translates as a shift in resonance frequency (Equation 2.2).

$$\frac{\Delta f}{f_0} = -\frac{1}{2}\frac{\Delta C}{C} \tag{2.2}$$

In a microwave resonator, the capacitance shift induced by a microparticle depends on the particle size and the dielectric permittivity difference between the particle and the medium, based on the following equation [65].

$$\Delta C = 4\pi\epsilon_{fluid} K_{CM} r^3 \frac{|E^2_{rms}(r_{particle})|}{U^2_{rms}} \tag{2.3}$$

Here, r is the particle radius, U_{rms} is the applied voltage,E_{rms} is the value of the electric field at the location of the particle. Clausius-Mosotti factor, K_{CM}, shows the difference between the dielectric permittivity of the medium and the microparticle (Equation 2.4).

$$K_{CM} = \frac{\epsilon_p - \epsilon_m}{\epsilon_p + 2\epsilon_m} \tag{2.4}$$

Positional dependency arises because the capacitance shift depends on the square of the electric field magnitude, which is non-uniform between the coplanar electrodes. As discussed, position dependency can be mitigated by using either parallel plate or 3D electrode configurations which yield a uniform electric field at the sensing region. Figure 2.1 shows the 3 aforementioned electrode configurations together with the electric field intensity at the sensing region: (a) coplanar electrodes (b) the electric field distribution at the sensing region, the magnitude of electric field changes along the microfluidic channel c) Parallel plate electrodes (d) the electric field at the sensing region which is uniform between the electrodes (e) Vertical, 3D electrodes (f) and the electric field at the sensing region, which is also uniform between the electrodes. Electrodes are shown by the yellow rectangles at the top panel. Colormap shows the magnitude of electric field (V/m) at the sensing region between the electrodes, for a voltage difference of 1V applied across the electrodes separated by 30µm in coplanar electrode geometry (a), (b) and 20 µm in parallel-plate (c), (d) and 3D electrode (e), (f).

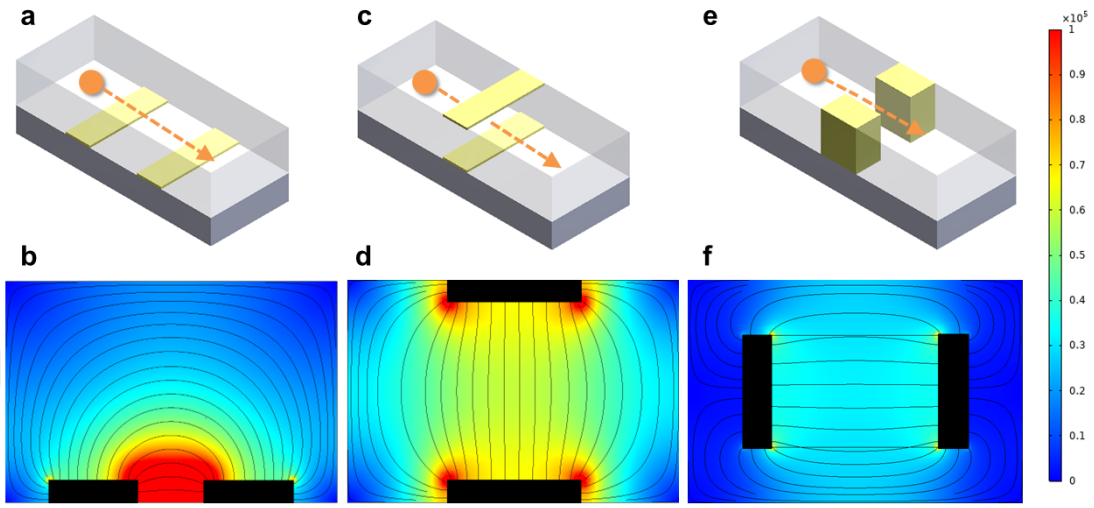

Figure 2.1: Electrode configurations in microfluidic sensors and the electric field intensity at the sensing region

For 3D electrode integrated microwave resonators, the capacitance shift depends only on the dielectric permittivity and the geometric size of the particle. Using Equation 2.3, the capacitance shift induced by 2 microparticle populations with different dielectric permittivity and size can be determined as follows (Equation 2.5).

$$\frac{\Delta C_1}{\Delta C_2} = \frac{K_{CM1} r_1^3}{K_{CM2} r_1^2} \tag{2.5}$$

It is not possible to distinguish microparticle samples with different sizes and dielectric permittivity based on only microwave signals. Optical microscope recordings of single particle passage events through sensing region can be processed simultaneously with the microwave signals to measure both electric and geometric volume of the microparticles [4]. Another approach is integrating a second sensor operating at low frequency (kHz-MHz regimes) at the sensing region of the microwave resonator [16]. Particle-induced electrical signal depends only on the geometric volume of the particle at low frequencies. In Chapter 5, low and high-frequency sensors are used together for the classification of different microparticle populations. The operation of low frequency sensor-Coulter Counter- is explained in the next subsection.

2.2 Microparticle Size Measurement with Coulter Counter Technique

Coulter counter method is commonly used in literature for microparticle/cell counting, sizing, and analysis in microscale due to its simplicity [1]. It has even been implemented for the analysis of nanoparticles [2]. In Coulter counter, a microfluidic channel is filled with an electrolyte solution, and a voltage difference is applied across the electrodes inside the microfluidic channel. A microparticle blocks the ionic current as it passes between the electrodes, and in turn, causes an impedance shift in the sensor which is reflected as a drop in the current. Change in current is inversely proportional to the geometric size of the microparticle.

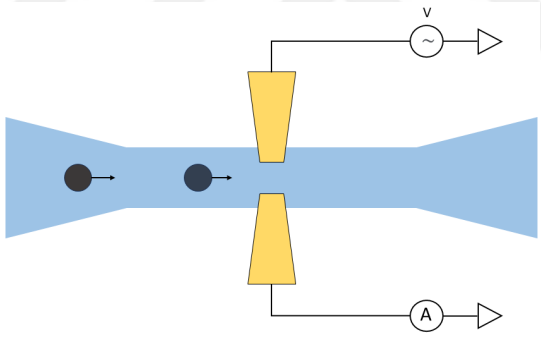

Figure 2.2: Schematic drawing of Coulter Counter

Coulter counter can be implemented by applying either DC or AC voltage to the excitation electrode. Using DC voltage only gives information about the particle size and number of particles passing through the channel while particle/cell characterization can be done through impedance measurement if AC voltage is applied.

Similar to microwave sensors, Coulter counters with coplanar electrodes also suffer from positional dependency which can be mitigated using the approaches described in Introduction. In Chapter 5, a Coulter counter with 3D electrodes is used together with the split ring resonator to measure the dielectric permittivity and geometric size of the microparticles simultaneously, without any post-processing for particle trajectory.

Chapter 3

Microparticle Sensing with Liquid Metal Integrated Microwave Resonators

In this section, 3D electrodes on the microwave resonator were obtained by injecting Galinstan inside the dead-end access channels perpendicular to the microfluidic flow channel. Design, fabrication, experiment procedure and data analysis are explained below.

3.1 Resonant Sensor Design

The designed sensor utilizes the concept of liquid electrodes to obtain a uniform electric field at the microfluidic channel integrated on a split ring resonator (SRR) operating at the microwave regime. The split ring resonator (Figure 3.1a) consists of 2 concentric rings: Due to inductive coupling, a standing wave is formed on the inner ring when the outer ring is excited. In the split ring resonator topology used in the study, the main resonating structure is the inner ring, which consists of a split region that is usually comparable to the size of an analyte particle ($\sim$

20µm). Here, the width of the gap region is increased to 360µm to incorporate the access channels. Figure 3.1 shows (a) a schematic drawing of the coplanar split ring resonator and (b) electric field at the sensing region of a split ring resonator with ring gap size 20µm (Adapted from [66])

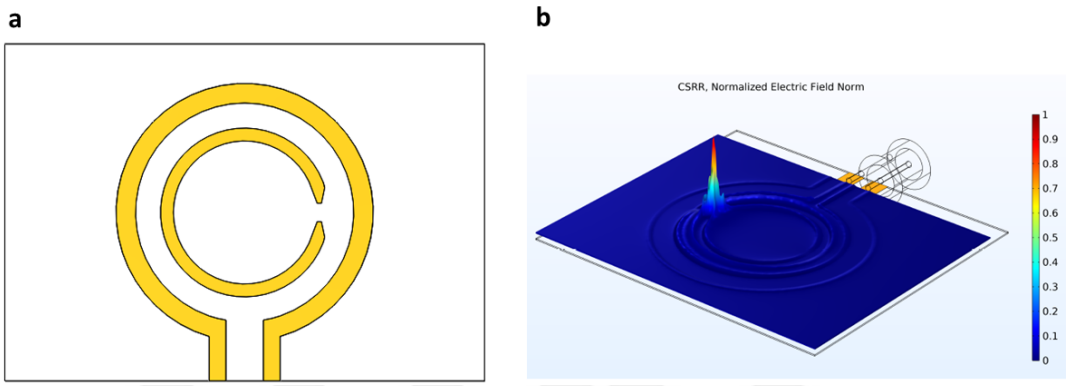

Figure 3.1: Coplanar split ring resonator design

Dead-end access channels were positioned at the sidewalls of the microfluidic channel, on top of the coplanar split ring resonator electrodes. Motivated by the need to develop a uniform electric field across electrodes at the microwave band, Galinstan is filled inside the access channels. The electric field formed between the coplanar electrodes of SRR is extended to form a uniform electric field inside the microfluidic channel due to the conductivity of Galinstan. Figure 2 shows the schematic drawing sensor: (a) Access channels filled with Galinstan on SRR, (b) magnified view of the sensing region (c) top view of the sensor (d) optical m microscope image of the sensing region containing the access channels filled with Galinstan and the microfluidic channel. The coplanar gold electrode is partially visible under the access channel

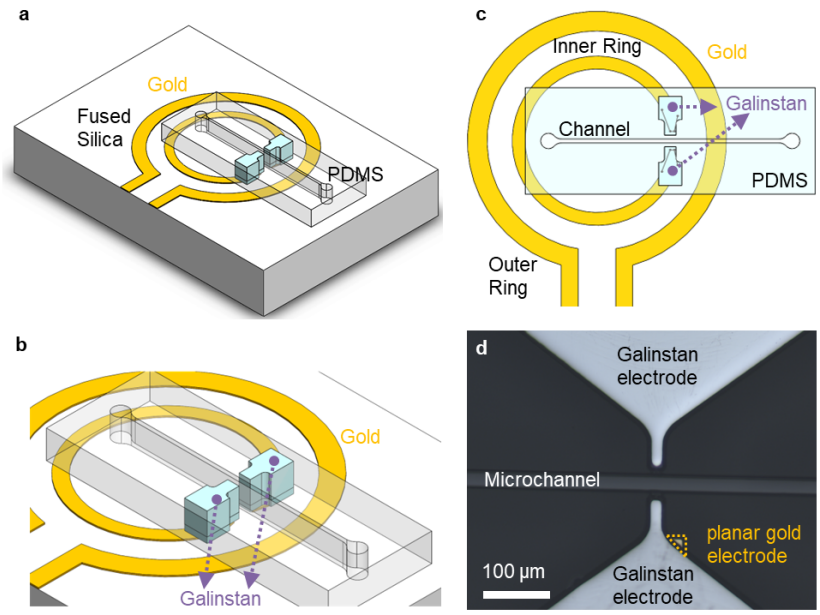

Figure 3.2: Schematic drawing and micrograph of the Galinstan integrated split ring resonator

The distance between the liquid electrodes at the sensing region decreases to 70µm at the sensing region. Since Galinstan is liquid at room temperature, PDMS spacers with 10µm width are positioned between the liquid electrode and microfluidic channel at both sides to prevent metal leakage from the access channel to the microfluidic flow channel.

3.2 Fabrication

Sensor fabrication was done in 2 steps: microwave resonator and microfluidic channel fabrication. A 4-inch fused silica wafer with 500µm was diced into half, using dicing saw. After cleaning each substrate with acetone, IPA, and DI water AZ 5214 photoresist was spin-coated at 2300 rpm, 300 acceleration for 40 seconds to a final thickness of 1.6µm. Soft-bake was done at 110°C for 80 seconds. Substrates were exposed to UV light to pattern the coplanar split ring resonator using the following exposure parameters: Soft contact, separation 100µm, constant time: 4 seconds (mask aligner dose: 29.5mJ/cm^2). Exposed substrates

were developed inside AZ400K solution (AZ400K: DI water ratio 1:4) for 40 seconds and rinsed with DI water, the sensing region of the developed pattern was controlled under the microscope. If the resonator pattern was underdeveloped, the substrates were kept inside the developer for 10-20 seconds more, until the pattern was developed properly.

Later, the substrates were put into thermal evaporator chamber for metallization of the resonator pattern. Initially, 10 nm of chromium was coated as an adhesion layer, followed by 120-130nm gold evaporation. Substrates were put into acetone for 1-2 hours for lift-off. Figure 2a shows the split ring resonator on fused silica after lift-off.

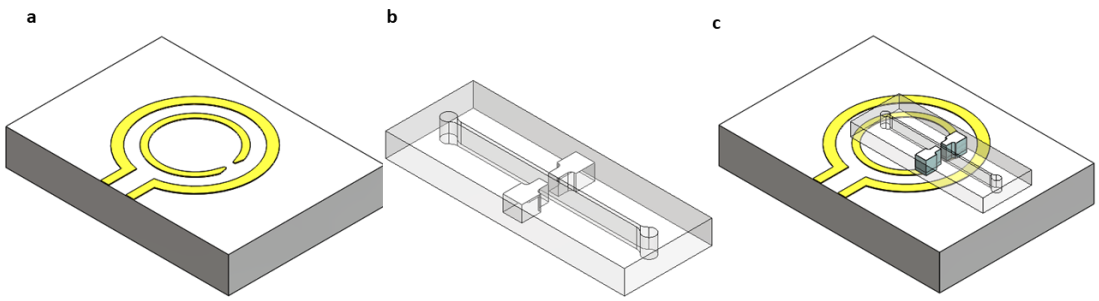

Figure 3.3: Fabrication steps of liquid electrode integrated split ring resonator

Microfluidic channel mold was fabricated on a 4-inch silicon wafer with 500µm thickness. The wafer was cleaned with acetone, IPA, and DI water and treated with oxygen plasma to increase the photoresist adhesion. SU8 2050 negative photoresist was spin-coated to a final thickness of 50 µm using the following parameters: Coating step 1: 500 rpm, 100 acceleration, 20 seconds, Coating step 2: 3400 rpm, 300 acceleration, 1 minute. Then, the wafer was soft baked at 65°C for 3 min, and at 95°C for 7 min, consecutively and cooled to room temperature before exposure to avoid thermal shock. Later, UV exposure was done under the microfluidic channel mask with the following exposure parameters: Proximity and separation 120µm, constant time 8 seconds (mask aligner dose: 29.5mJ/cm^2). Exposed wafer was put on hot plate for post-exposure bake with the same duration and temperature as the soft-bake step and developed inside

Kayakuam SU8 developer solution for around 10 minutes till there were no white residues upon IPA rinse. The region between the access channels and microfluidic flow channel was checked under an optical microscope to check if PDMS spacer was properly patterned. Then, the developed wafer was put on hot plate at 140°C for 1 hour to hard bake the SU8 and further improve its adhesion on the Si wafer. To fabricate the microfluidic channels, PDMS (Sylgard 184) was mixed 10:1 ratio (base: curing agent) and degassed inside the dessicator. PDMS was poured on the hard-baked wafer and left to cure on hot plate set to 100 °C for 40 minutes. The microfluidic channel was peeled from the mold. Figure 2b shows the PDMS microfluidic channel and the access channels. Microfluidic channel with access channels was bonded on the resonator, aligning the access channels on top of the coplanar split ring resonator electrodes after oxygen plasma treatment using the parameters: 100W, 2 minutes, 50 sccm O_2 flow.

The last step of fabrication was the injection of Galinstan into the microfluidic access channels. Liquid metal is filled into an injector(1CC injector, 26 G x $\frac{1}{2}$" needle) from the bottle. While developing the fabrication procedure, it was observed that liquid metal could easily leak into the microfluidic flow channels even though there was PDMS spacer, so Niobium magnets were fixed on top of the microfluidic channel and at the bottom of the fused silica wafer to improve the adhesion of the channel before Galinstan injection. Galinstan was injected very slowly and the amount of Galinstan inside the access channel was continuously monitored under the optical microscope. Figure 2c shows the microfluidic channel and split ring resonator at the end of the fabrication.

3.3 Experiment Procedure

The experiment setup used for polystyrene microparticle size classification experiments had 3 subcomponents:

1. Custom-built, phase-sensitive detection circuit to track the phase and amplitude response of the microwave resonator

2. Pressure control system (Fluigent MFCS-EZ) and fluid reservoir to introduce the fluid carrying the analyte microparticles inside the microfluidic channel

3. Optical microscope to monitor single particle passage events from the sensing region

During microparticle sensing experiments, the resonator was mounted to custom-built electronic circuitry. The sample solution containing polystyrene was prepared by mixing 15µL of 30 and 20 µm (Serial numbers: 74491, 84135, respectively) microparticles inside 10 mL DI water. Tween 20(0.1% concentration) surfactant was added to the solution to avoid agglomeration and microfluidic channel clogging.

After filling the microfluidic channel with the solution, the resonance frequency of the resonator was determined by doing an open loop frequency sweep with the electronic circuit. Sensitivity of each prospective resonance frequency was checked by passing several particles back and forth. The phase and amplitude of the resonator were tracked in an open-loop measurement configuration. As microparticles were passing through the sensing region between the Galinstan electrodes, they induced a capacitance shift which was translated to a shift in resonance frequency. Particle-induced shifts were reflected as a spike-shaped jump in phase and amplitude signals simultaneously. Additionally, the particle passage events from the sensing region were recorded with the optical microscope to verify the microwave signal and correlate the signals with different-sized particles. Events due to multiple particles and clusters were also excluded based on optical microscope recordings.

3.3.1 Electronic Measurement

Resonance characteristics (resonance frequency and quality factor) of the microwave resonator were measured using a vector network analyzer (VNA) before starting an experiment. Figure 3 shows the amplitude response of the resonator

before and after filling the access channels. Resonance frequency shifted significantly and the quality factor increased after filling the access channels as a result of the increased capacitance at the sensing region. The quality factor was calculated using the 3-dB bandwidth method.

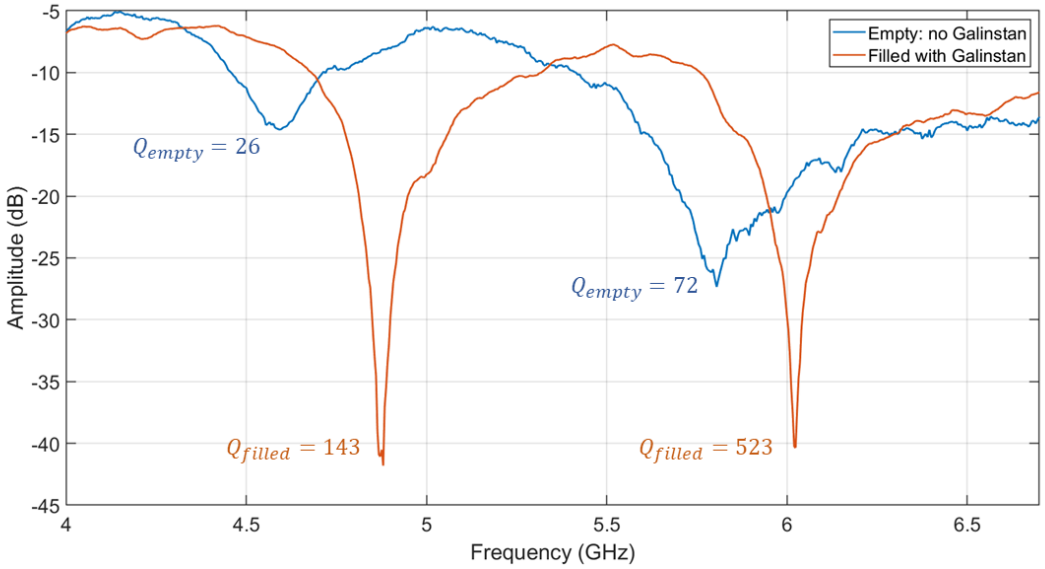

Figure 3.4: VNA amplitude response of SRR before and after Galisntan filling

Electronic measurement was done by narrow-band phase-sensitive detection circuitry composed of a signal generator and two lock-in amplifiers (Figure 3.5).Upper frequency limitation of the lock-in amplifier (5MHz) requires an external heterodyne RF circuitry operating around the resonance frequency of the resonator (6-6.5GHz) [67]

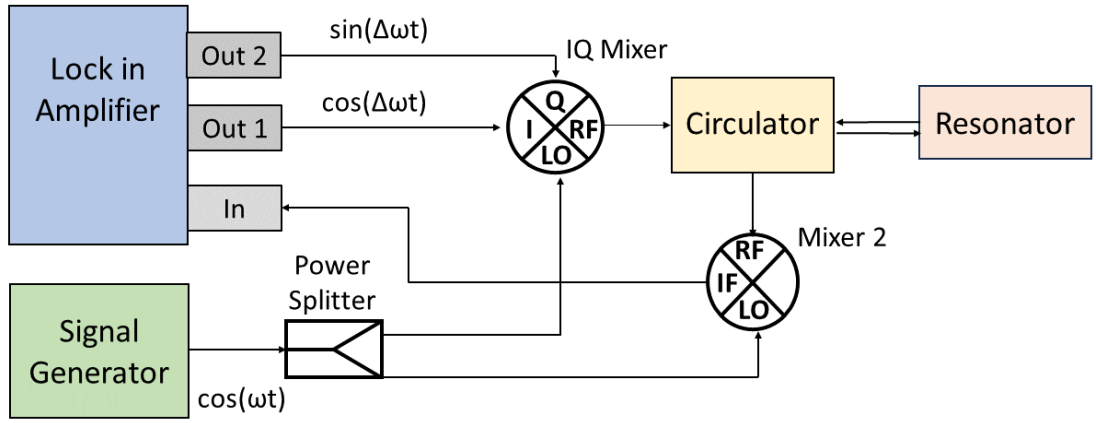

Figure 3.5: Electronic circuit used to track the phase and amplitude of the microwave resonator

The circuitry was configured to track the changes in phase and amplitude, induced rapid microparticle passage event from the sensing region hence no additional calibration steps are employed. Internal oscillator of the lock-in amplifier was used to generate the reference signal required for phase-sensitive detection. The reference signal was up-converted to GHz range, and supplied to the resonator and the reflected signal carrying the phase and amplitude information of the resonator was down-converted to the operational range of the lock-in amplifier. Single sideband modulation was employed for upconversion, using two lock-in amplifiers. Frequency upconversion results in two frequencies, $\omega + \Delta\omega, \omega - \Delta\omega$, IQ mixer was used to cancel out one of the sidebands. Two reference signals with 90°C were generated by the lock-in amplifiers. The signal at the resonance frequency was supplied to LO port of IQ mixer from the signal generator. The resultant signal from IQ mixer, at the difference of LO and lock-in reference frequency, was fed to the resonator using a circulator. The reflected signal from the resonator was down-converted to the operation range of the lock-in amplifier using a mixer. Later, the phase and amplitude of the resonator were digitally read using LabOne software.

3.4 Data Analysis

Analyte microparticles induced simultaneous phase and amplitude shifts in the microwave resonator. The out-of-phase component of the reflected signal from the resonator (Y-quadrature, ($Y = Rsin(\theta)$) is proportional to the capacitance change due to a particle (Equation 3.1)

$$\Delta Y \propto \frac{\Delta C}{C} \tag{3.1}$$

Taking the derivative of the constitutive equation, ΔY parameter can be expressed using phase and amplitude values using Equation 3.2.

$$\Delta Y = \Delta R sin(\theta) + R cos(\theta) \Delta\theta \tag{3.2}$$

A custom-built MATLAB script was used to detect the particle-induced phase and amplitude shifts and analyze their magnitude. The first step of data analysis was the removal of the long-term drift in the raw phase and amplitude signals by baseline reduction using the MATLAB function *msbackadj*. Long-term drift was observed because no control loop was employed in the measurement. Later, the magnitude and location of particle-induced peaks were determined on baseline reduced phase signal using the built-in MATLAB function *findpeaks*. A peak prominence threshold was assigned to differentiate between noise and events based on the noise level from data sets without any particle events. Signal-to-noise ratio (SNR) was usually better in phase signal so event locations were initially determined on phase data. Later, simultaneous events in amplitude and phase were matched based on peak location.

Finally, raw values of phase and amplitude signals from the baseline signals were used together with the magnitude of particle-induced shifts to calculate the Y-quadrature. For data sets containing particle populations with different sizes, histograms of phase, amplitude shifts and ΔY showed bimodal distribution. K-means algorithm was used to divide the bimodal distribution into unimodal distributions and calculate the mean, standard deviation, and coefficient of variation for each population.

3.5 Experiment Results

3.5.0.1 Polystyrene Particle Size Classification Experiments

Figure 3.6 shows phase and amplitude shifts during the passage of 20- and 30-µm microparticles together with the optical microscope images of the sensing region. Since both particles were polystyrene, microwave signals were proportional to the size of the microparticles.

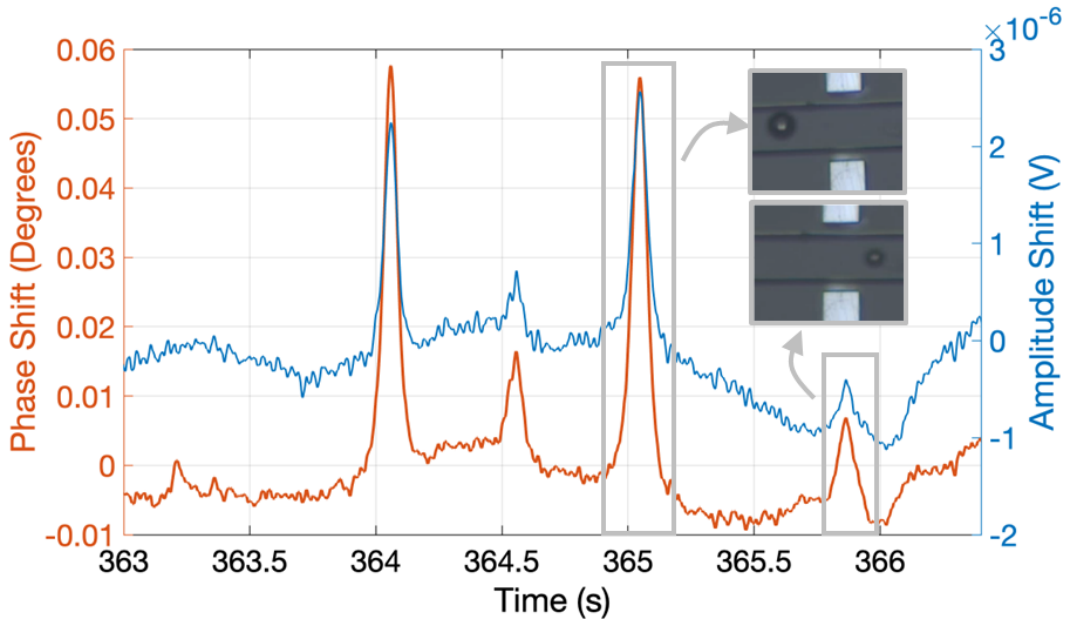

Figure 3.6: Particle-induced phase and amplitude shifts on raw data

Later, the Y-quadrature shift histogram was plotted for a data set containing 887 single particle events (Figure 3.7). The histogram showed a bimodal distribution, where the respective peaks corresponded to 20 and 30µm particles. Using the K-means algorithm, a unimodal distribution fit was obtained for each population.

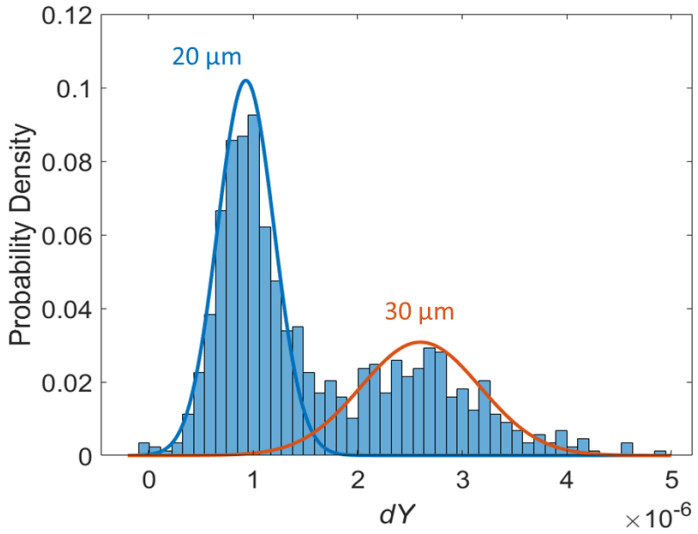

Figure 3.7: Y-quadrature shift histogram of 20 and 30µm polstyrene particles

Statistical parameters for each unimodal distribution are shown in Table 1.

	20-µm Particles	30-µm Particles
Mean	$9.3x10^{-}7$	$2.6x10^{-}6$
Standard deviation	$2.7x10^{-}7$	$5.7x10^{-}7$
Coefficient of variation	0.29	0.21

Table 3.1: Statistical parameters for 20- and 30-µm particles

By using liquid electrodes, positional dependency is mitigated; same particles induce the same signal regardless of their position inside the microfluidic channel.Microwave signals are proportional to particle volume, as indicated by the phase and amplitude shifts. Here, the ratio of mean Y-quadrature shifts between 30 to 20µm particles is 2.8 while the volume ratio of the particles is 3.4.

Chapter 4

Microparticle Size Classification Experiments with SU8 Microelectrode Integrated Microwave Resonators

The second approach for integrating 3D electrodes on a microwave resonator is based on the use of metalized SU8 pillars as a structural material for 3D electrodes. SU8 microelectrodes are electrically connected to a microstrip transmission line resonator through wirebonds, so the electric field on the resonator is extended to form a uniform electric field inside the microfluidic channel between SU8 electrodes. Polystyrene microparticle size classification experiments were conducted with this architecture.

4.1 Resonant Sensor Design

The sensor structure is composed of 3 subcomponents: (i) Microstrip transmission line microwave resonator on a PCB and a separate sensing region on a fused

silica chip including (ii) SU8 microelectrodes on coplanar gold electrodes and (iii) PDMS microfluidic channel. The sensing element of the structure is the microwave resonator (Figure 1): There are 3 strips on the PCB and the resonator is formed by the middle line and the ground pad at the bottom of the PCB. Strips on the side are used for excitation and readout. Using the microwave resonator, changes in capacitance are translated into changes in resonance characteristics measured accurately using phase-sensitive detection.

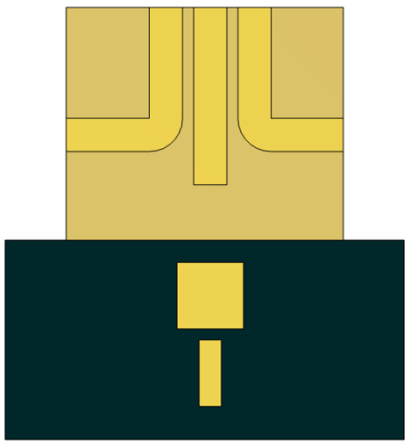

Figure 4.1: Microstrip transmission line resonator

Coplanar electrodes on the fused silica substrate are used to achieve an electrical connection between the microwave resonator and 3D electrodes. During the microfabrication process, 3D electrodes are patterned at the tip of the coplanar electrodes, which are later connected to the resonator via wirebonds. As a result of the wirebonds and the electrical contact between coplanar and 3D electrodes, the electric field formed on the resonator is extended to form a uniform electric field between the SU8 microelectrodes along the microfluidic channel. Figure 2 shows (a) the subcomponents of the microwave sensor: The resonator and the fused silica chip with SU8 microelectrodes and the microfluidic channel (b) an optical microscope image of the sensing region (c) a schematic drawing of the sensing region and the electric field inside the microfluidic channel.

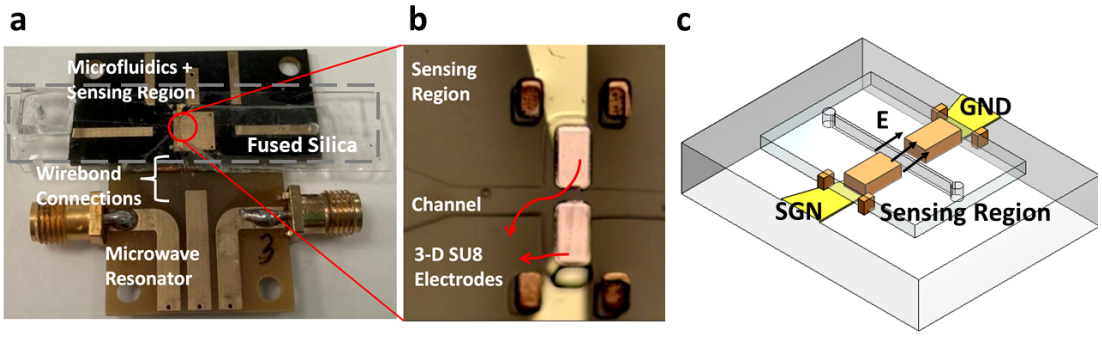

Figure 4.2: Images and schematic drawing of the microwave resonator sensor and its sensing region

4.2 Fabrication and Characterization

Fused silica chip with the microfluidic channel, 3D SU8 microelectrodes, and the underlying coplanar electrodes was fabricated in the cleanroom and later bonded on the microwave resonator. The first step of fabrication was dicing a 4-inch, 500µm thick fused silica wafer to 1x5cm substrates. Initially, coplanar electrodes were patterned on each chip and coated with Cr/Au using the photolithography and thermal evaporation recipe explained in Chapter 3.2 (Figure 4.3 a).

The first step for the fabrication of SU8 pillars that would serve as the structural material for 3D electrodes was spin coating SU8-2050 photoresist with a final thickness between 45-50µm using he following recipe: Step 1: Spin speed 500 rpm, acceleration: 100, 20 seconds; Step 2: Spin speed: 3500rpm, acceleration: 300, 1 minute. After spin-coating, substrates were baked at 65 and 95 °C for 3 and 7 minutes, respectively. After each baking step, substrates are left to gradually cool down to room temperature to avoid any thermal stress that can affect the surface roughness of the electrodes. Substrates were exposed to UV light to pattern the SU8 pillars at the tip of the coplanar electrodes with the following exposure parameters: Soft contact mode, separation: 120 µm, constant time: 11.5 seconds (mask aligner dose: 29.5mJ/cm^2). Optimization of the UV dose was one of the most critical steps in the fabrication: In case of under or over-exposure, the wall profile of SU8 electrodes becomes slanted, affecting the uniformity of the electric field inside the microfluidic channel. The wall profile of

the SU8 microelectrodes was checked using scanning electron microscopy (SEM) to control the exposure dose. After UV exposure, substrates were put on the hot plate for post-exposure baking at the same temperature and for the same duration as the previous baking step. SU8 micropillars were developed inside the developer solution (Kayakuam) until there were no white residues on the substrate upon rinsing with IPA. The development of the micropillars and the alignment with the coplanar electrode layer was controlled using optical microscope. In case of any misalignment or change in exposure dose, SU8 was removed from the substrate inside acetone using ultrasonication. Otherwise, SU8 was hard baked on hot plate at 140°C for 1 hour to increase its adhesion to the substrate. Figure 4.3b shows the SU8 pillars at the tip of the coplanar electrodes.

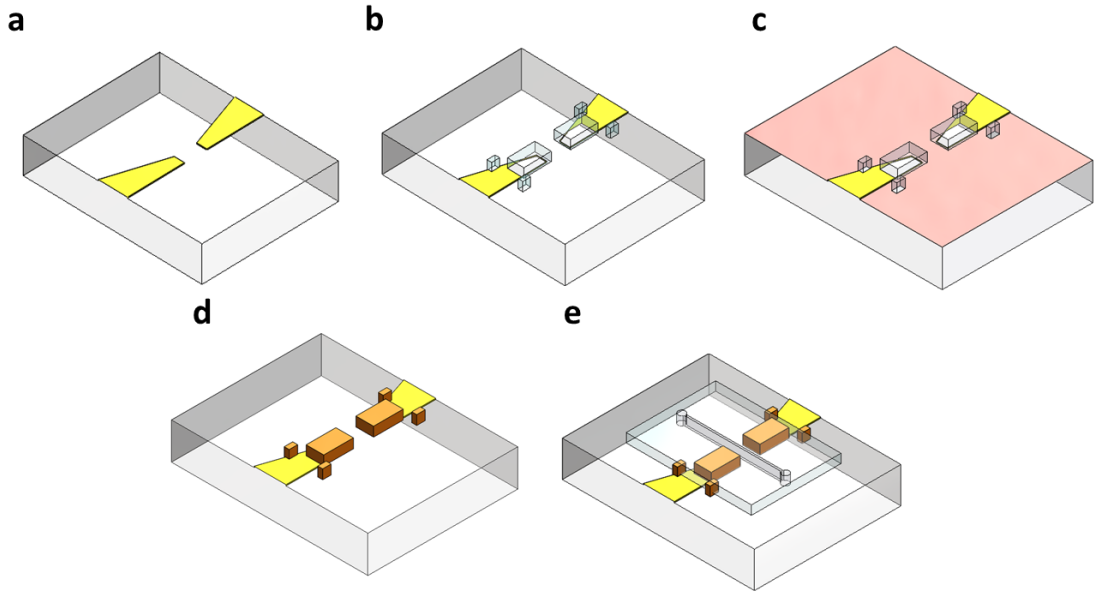

Figure 4.3: Fabrication procedure of 3D electrodes on fused silica substrate

Metalization of SU8 micropillars was done in 2 steps: First, a layer of AZ5214E positive photoresist was spin-coated to a final thickness of 1.6µm to obtain a lift-off layer covering everywhere except for the 3D electrodes (Figure 4.3c). Before deposition, substrates were cleaned using oxygen plasma treatment for 2 min, using 83W power and 25 sccm O_2, 10 sccm N_2 flow to remove any particle or dust

that might cause difficulty for lift-off. An Aluminum or Chromium layer was conformally coated on the SU8 pillars using DC sputter deposition. Substrates were mounted on 45°tilted SEM stub during the deposition to prevent any shadowing effect that would cause non-uniform coating at the inner/outer surface of the pillars. Sputter deposition was done using the following parameters: 100W DC power at 1E-3 torr with 20sccm Ar flow, with substrate rotation for 10 minutes. Sputtering step was repeated twice for each substrate, after chancing their tilt direction by 180°to coat the inner/outer walls of opposite SU8 pillars. Substrates were put in an acetone bath for lift-off for 1-2 hours. In case of any lift-off problem, substrates were put in an ultrasonic bath inside acetone for 5-10 seconds to remove any adherent metal on the surfaces where metal was not intended. Figure 4.3d shows metalized SU8 pillars after lift-off. Finally, the PDMS microfluidic channel was fabricated and bonded on the substrate after oxygen plasma treatment using the same recipe as Chapter 3.2. Figure 4.3e shows the fused silica chip after fabrication.

While developing the fabrication protocol, SU8 pillars were characterized using SEM to measure the thickness of the pillar, wall profile, and the uniformity of the metal deposition. Figure 4.4 shows the SEM images of the 3D electrodes on the coplanar gold electrodes. An additional layer of platinum/gold was deposited to avoid any charging during imaging.

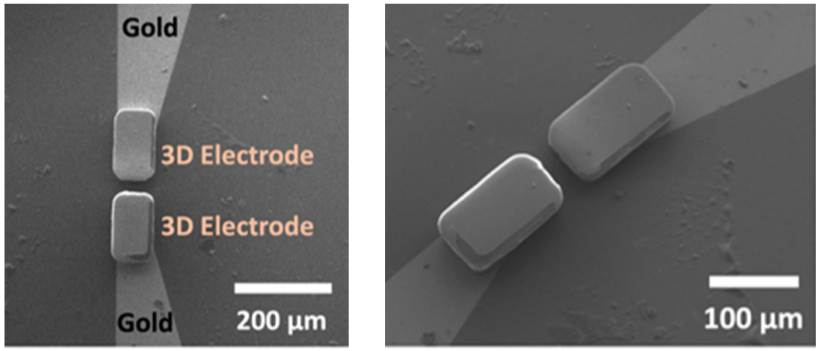

Figure 4.4: SEM images of SU8 microelectrodes on coplanar gold electrodes

4.3 Experiment Procedure

SU8 microelectrode integrated resonator architecture was used for size classification experiments with 12- and 20 µm PS microparticles. The solution containing analyte microparticles was prepared by mixing 15µL 12 µm polystyrene (Part number: 88511, Sigma Aldrich) and 20 µm polystyrene (Part number: 744911, Sigma Aldrich) solutions inside 10mL PBS solution (Biowest). Tween 20 (Sigma Aldrich) surfactant was added to the solution (0.1%) to avoid microfluidic channel clogging. Similar to Chapter 3, the experiment setup was composed of custom-built electronic circuitry, a pressure pump, and an optical microscope. Due to the resonance frequency of the resonator, the IQ mixer could not be employed in the electronic circuit. Details of electronic measurement are explained below.

4.3.1 Electronic Measurement

The resonance characteristics (resonance frequency and quality factor) of the resonator with and without the metalized SU8 microelectrodes were measured using VNA (Figure 4.5).

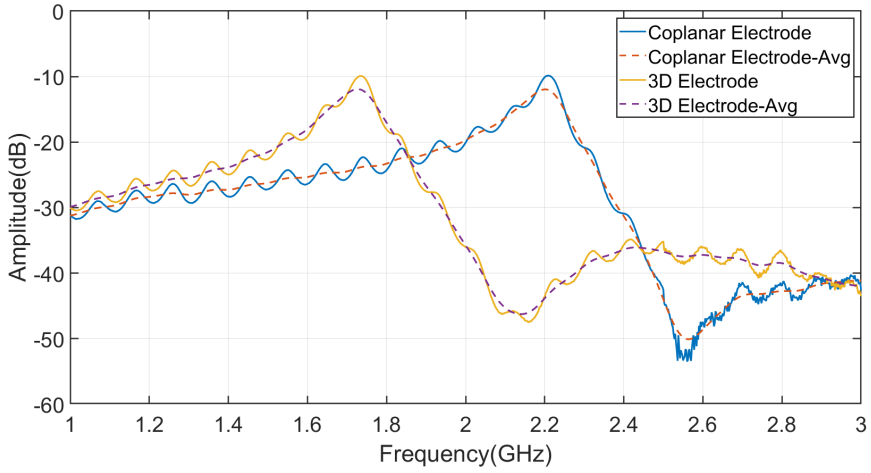

Figure 4.5: Amplitude response of the microstrip transmission line resonator

The resonance frequency of the resonator with coplanar electrodes at the sensing region was around 2.1 GHz. Sensing region capacitance increased due to the presence of 3D electrodes, causing the resonance frequency to decrease around 1.7GHz. VNA response contains undulations due to high reflections in the device, dashed lines on the plot show the response after curve smoothing by averaging.

The electronic circuitry described in Chapter 3.3 2 was based on single sideband measurement topology using an IQ mixer which operates between 2-18GHz. Here, since the resonance frequency of the microwave resonator was below 2 GHz, a double-sideband measurement topology, involving a double-sideband modulator, was used in the measurements. Figure 4.6 shows the electronic circuitry used for microparticle sensing experiments [68].

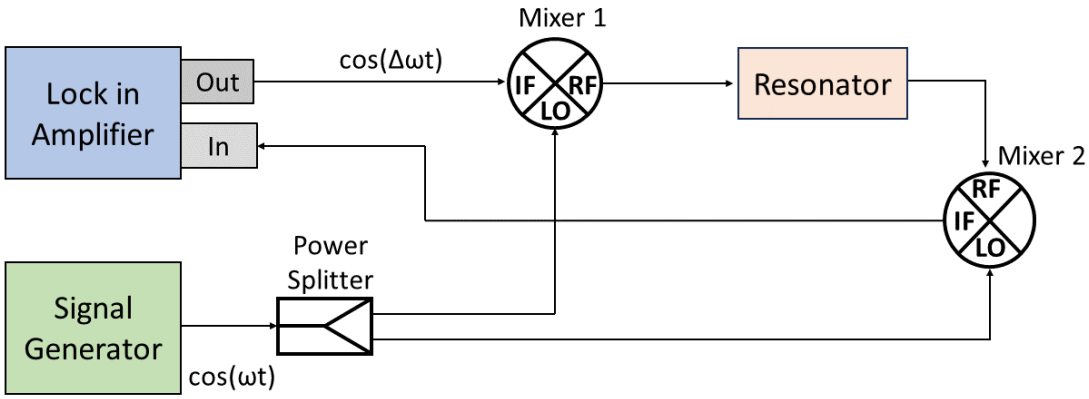

Figure 4.6: Electronic circuit for polystyrene microparticle sensing experiments with microstrip transmission line resonator

Similar to Chapter 3.3, the internal oscillator of the lock-in amplifier was used to generate the reference signal required for phase-sensitive detection. This time, instead of 2 reference signals with 90°C phase difference, a single reference signal was used in the circuit. Local oscillator (LO) signal was supplied from the signal generator which was set to the resonance frequency of the resonator. Since the microstrip transmission line resonator was a 2-port device, a circulator was not employed in the circuit. The signal from the resonator was down-converted to lock-in amplifier operation frequencies and fed to the lock-in amplifier. Phase and amplitude (R and Θ)) of the signal reflected from the resonator were digitally

recorded for further analysis. During the experiments, a lock-in time constant of 1 ms and a data transfer rate of 13.4kSa/s were used to increase the signal-to-noise ratio and measure particles with high velocity.

4.4 Data Analysis

Several steps regarding signal processing were added to the MATLAB code described in Section 3.4 to increase the peak finding accuracy of the code. Fourier transform of the time domain signals was calculated and power line noise components and their harmonics were removed using a combination of notch filters. As a result of positioning SU8 microelectrodes inside the microfluidic channel, high SNR ($\sim$ 40 for 20µm PS microparticles) was obtained in the experiments yet, to reduce any uncertainties, the square of the baseline reduced amplitude signal was used peak finding. The peak threshold was again assigned based on the noise level on a data set with no events. Later, the square root of the peak magnitude was calculated to normalize the magnitude of the shifts. After peak normalization,the code was same as the one in Chapter 3.4. Due to the increase in SNR, histograms from experiments involving multiple particle populations showed 2 unimodal distributions rather than a bimodal distribution, so statistical parameter of each population was calculated separately.

4.5 Experiment Results

SU8 microelectrode microwave resonator architecture was used for polystyrene microparticle sensing experiments. Figure 4.7 shows the 20µm particle-induced amplitude shifts obtained using (a) coplanar and (b) 3D electrodes measured using the same electronic circuitry. The coplanar sensor was a split ring resonator with a sensing gap of 20µm between 100nm thick gold electrodes. Although the particles had uniform size distribution and were made of the same material, positional dependency caused significant variation in the signal. For the case with

3D electrodes, due to the uniform electric field magnitude of the signal was the same regardless of the particle position inside the microfluidic channel. The gap between SU8 electrodes at the sensing region was 120µm.

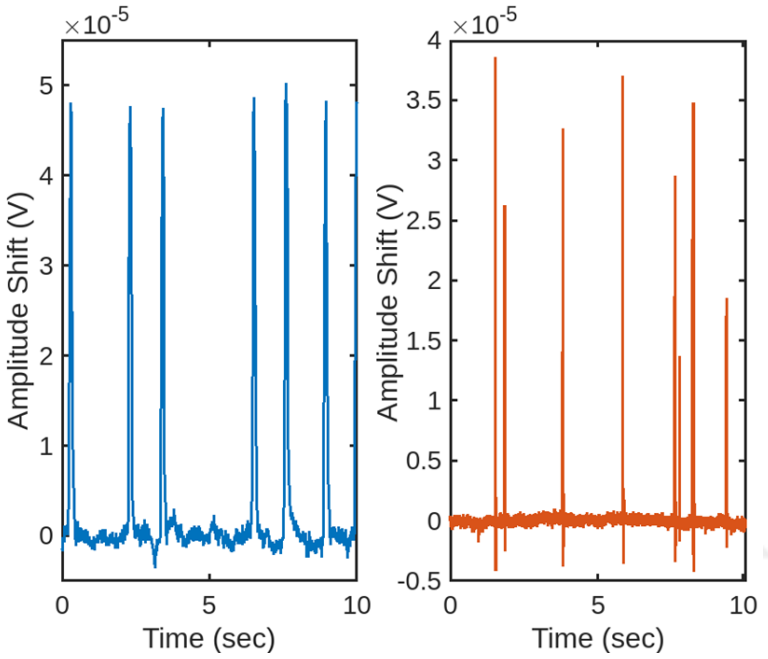

Figure 4.7: Amplitude shifts recorded for 20µm PS microparticles using (left) 3D microelectrodes (right) coplanar electrodes.

SU8 microelectrode-integrated resonators were further used for size-classification experiments between 12- and 20-µm polystyrene particles. A solution containing both 12-and 20-µm particles was passed through the microfluidic channel. Figure 4.8 shows the phase and amplitude shifts induced by single 12- and 20-µm particles on baseline reduced signals. Two different signal levels indicate the presence of two particle populations. Red and black dots show the magnitude of shifts induced by 20 and 12 µm particles, respectively. Since both particles were polystyrene, signal levels are proportional to particle volume.

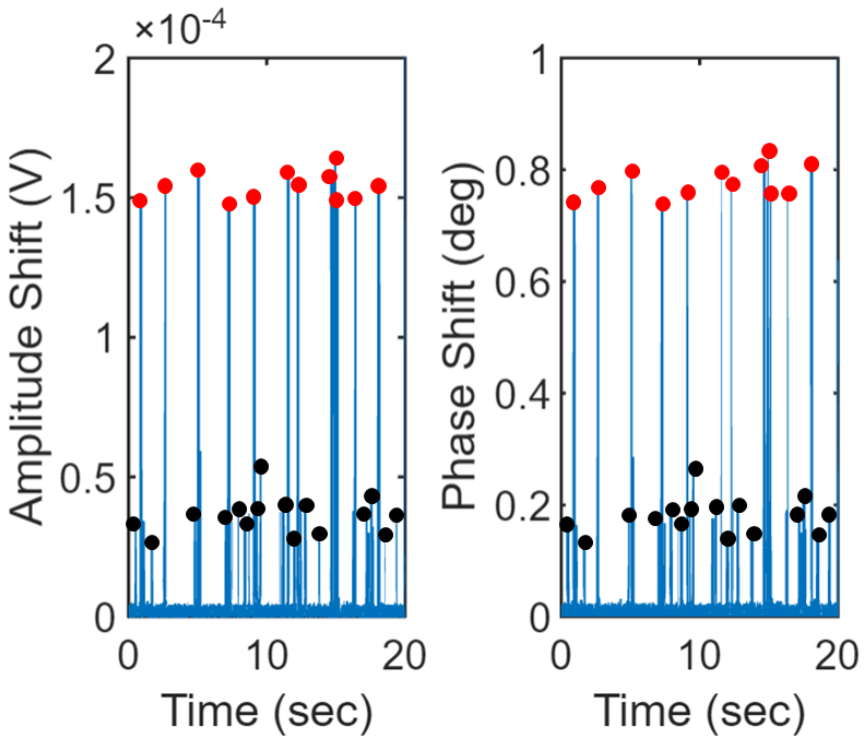

Figure 4.8: Phase and amplitude shifts on the baseline reduced signals corresponding 12 and 20µm microparticles

Phase and amplitude shifts were used to calculate the Y-quadrature shift for a population containing 369 microparticles (Figure 4.9). There is a clear distinction between the peaks, obtained without any post-processing to compensate for particle trajectory inside the microfluidic channel, indicating the presence of a uniform electric field between the SU8 microelectrodes. The ratio of mean Y-quadrature shift between 20 and 12µm particle peaks was calculated as 4.4 from the experiment while the volume ratio between the particles is 4.6. The same ratio was calculated as 4.4 and 4.6 using amplitude and phase shifts, respectively.

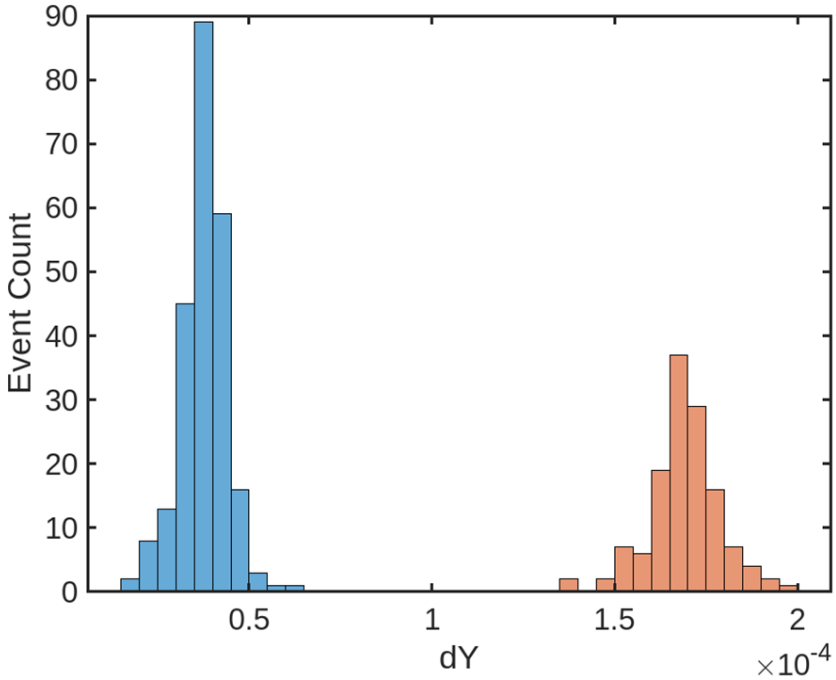

Figure 4.9: Histogram of Y-quadrature shift for 12-and 20µm polystyrene microparticles

Table 1 shows the statistical parameters (mean, standard deviation and coefficient of variation) for the Y-quadrature shift.

Particle Size	12-µm	20-µm
Mean	$3.8x10^{-}5$	$1.7x10^{-}4$
Standard deviation	$6.3x10^{-}6$	$9.8x10^{-}6$
Coefficient of variation	0.17	0.06

Table 4.1: Statistical parameters for 12- and 20-µm particles

Chapter 5

Microparticle Differentiation Experiments with SU8 Microelectrode Integrated Split Ring Resonators

In this section, microwave and Coulter counter sensors are integrated on a single chip to categorize microparticle species with different dielectric permittivity and size. Coulter counter electrodes are positioned at the sensing region of the split ring resonator. SU8 microelectrodes are fabricated at the tip of both the Coulter counter and split ring resonator electrodes to mitigate positional dependency in both sensors.

5.1 Sensor Design

The sensor architecture is a combination of a split ring resonator operating at microwave regime and a Coulter counter operating at low frequency, typically

around several hundred kHz. A microparticle is consecutively measured by microwave and Coulter sensors at the sensing region. Microwave signal depends on both the dielectric permittivity and the size of the particle while Coulter signal only depends on the particle size due to Debye shielding at low frequencies. Metalized SU8 electrodes are located at the tip of both microwave and Coulter counter electrodes at the sensing region inside the microfluidic channel so that the electric field between the coplanar electrodes can be extended to form a uniform electric field along the microfluidic channel. Figure 5.1 shows the split ring resonator and the Coulter counter electrodes (left) and the positioning of metalized SU8 microelectrodes on the coplanar electrodes inside the microfluidic channel at the sensing region (right).

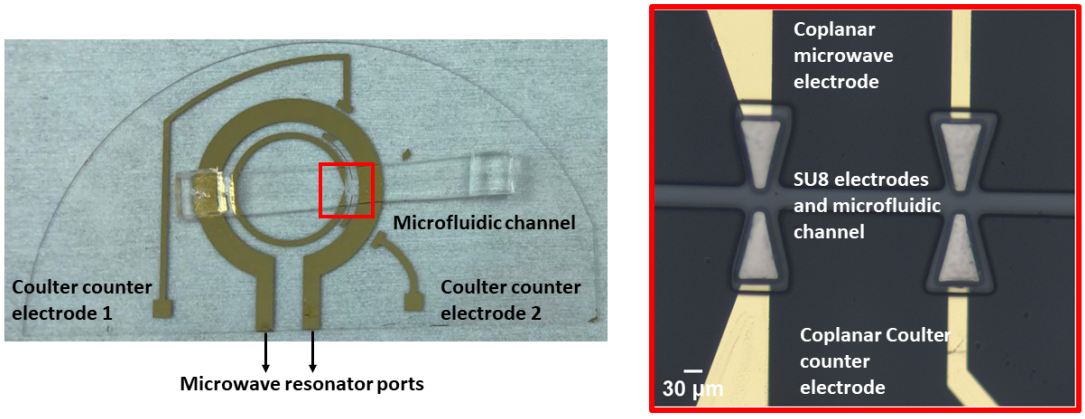

Figure 5.1: Sensor architecture: split ring resonator and Coulter counter (left) and optical microscope image of the sensing region (right)

Electrodes of the microwave resonator and Coulter counter are separated by 300µto avoid coupling between the electrical signals while ensuring the same particle is measured by both sensors consecutively. Coulter counter electrodes extend between the concentric resonator rings and are connected to excitation and readout pads at the left and right sides of the resonator through wirebonds. An SMA connector is soldered to one end of a copper wire and the second end of the wire is soldered to the Coulter counter pads.

5.2 Fabrication and Characterization

The fabrication procedure of the sensor is very similar to the method described in Chapter 4.2. A 4-inch, 500µm thick fused silica wafer was diced into two equal substrates using dicing saw. The first step of fabrication was patterning coplanar SRR and Coulter counter electrodes through the photolithography process. The pattern was metalized using a thermal evaporator by depositing 120nm Gold on a 10 nm Chromium adhesion layer. Coplanar electrodes were obtained after acetone lift-off.

SU8 pillars, which serve as the structural material for the 3D electrodes were patterned at the tip of the SRR and Coulter counter electrodes, forming the sensing region. SU8-2050 was spin-coated on the substrate and exposed to UV light after soft baking under the SU8 electrode mask. There were several designs for SU8 microelectrodes such as trapezoidal, thin, and straight electrodes (Appendix). After development and hard baking, a positive photoresist layer was patterned under the same mask used for SU8 electrodes to obtain a lift-off layer after SU8 electrode metalization. AZ5214E photoresist was spin-coated using 3000rpm, 300 acceleration, and for 40 seconds. The final thickness of the photoresist was around 1.4µm at this step, less than the resist thickness used for patterning the coplanar electrodes so that resist can spread easily between the 3D electrodes at the sensing region. Before SU8 electrode metalization step, oxygen plasma cleaning was done to remove any dirt or dust that could cause difficulty for lift off.

The last step of sensor fabrication was the metal deposition on SU8 pillars. Most critical aspect of this step was to obtain a conformal deposition profile on the SU8 pillars to form a uniform electric field inside the microfluidic channel. Although sputter coating yielded a conformal deposition profile, it was not suitable for lift-off because the deposition profile did not leave any area for acetone to enter and remove the resist and the unwanted material. Usually, metal remained on certain areas of the resonator surface, and ultrasonication was used to remove the unwanted metal that couldn't be removed during acetone lift-off.

In addition, the only targets available for sputter deposition were Aluminum and Chromium, which are susceptible to oxidation, decreasing the performance of the sensor during operation.

As an alternative, SU8 microelectrodes were coated with gold through thermal evaporation. The main advantages of using gold were its stability and superior conductivity. Furthermore, SU8 could act as an adhesion layer for gold, so it could be deposited without the need for an additional adhesion layer [69]. Gold can not adhere to fused silica without an adhesion layer, which makes the lift-off process easier compared to using Aluminum or Chromium. Yet, the coating profile obtained by thermal evaporation is not generally as conformal as the profile obtained with sputter deposition. The substrates were tilted 45 °on the thermal evaporation holder so that a conformal deposition profile could be obtained on the inner and outer walls of the SU8 electrodes. In both techniques, deposition is repeated twice to coat the walls of the SU8 electrodes on opposite sides. After the first deposition, the chamber was vent and the tilt direction of the substrates was changed. Details of each evaporation procedure are explained below:

1. **Thermal evaporation:** The most critical aspect of thermal evaporation is preventing excessive heating of SU8 electrodes during deposition, which can damage the structure of the photoresist. Upon excessive heating of SU8, the structure of the electrodes was damaged or they appeared black on the optical microscope, which might indicate carbonization of the structure during gold deposition. The coating rate should not exceed 0.4A/s during deposition to prevent excessive heating of SU8 and the associated problems. The process parameters were as follows: chamber pressure: $5x10^{-}5$ Torr, gold thickness at each deposition: 40-45nm.

2. **Sputter:** Thickness of the coating could not be monitored in sputter deposition so, before coating the actual sample, dummy substrates were coated to measure the coating rate. Deposition parameters were as follows: chamber pressure: 1E-3 Torr, DC power: 100W, deposition time: 10 minutes, Ar: 20sccm. At each step, the deposition thickness was approximately 100nm.

Finally, the substrates were put inside acetone lift-off for around 2 hours and checked under microscope.

Microfluidic channel mold fabrication started with coating SU8 2050 on a Silicon wafer with a final thickness of 50 µm. The spin speed at the second step was 3400 rpm, less than the spin speed used for the SU8 electrode step so that the microfluidic channel height is greater than the 3D electrodes and no air gap remains between the SU8 electrodes and the channel upon bonding. SU8 was exposed to UV light under the microfluidic channel mask after soft baking and put on hot plate for post-exposure bake afterwards. Finally, PDMS was poured on the mold after hard baking, cured and the PDMS channel was peeled off from the mold upon solidification. PDMS channel was bonded on the resonator after oxygen plasma treatment. Oxygen plasma treatment was done using 350W power, 40 seconds, 40sccm 0_2 and 10sccm N_2 flow. The microfluidic channel was aligned on the SU8 microelectrodes under optical microscope.

5.3 Experiment Procedure

Similar to Chapters 3 and 4, the experiment setup consisted of (i) Custom-built electronic circuitry for excitation and readout of the low and high-frequency sensors (ii) a pressure pump for transferring the solution containing analyte microparticles into the channel, and (iii) an optical microscope. The solution containing analyte microparticles was prepared by mixing powder polystyrene (PS) Cospheric, PSMS-1.07 14-20um - 500mg) or polyethylene microparticles(Cospheric, WPMS-1.45 10-20um - 0.1g) inside 10mL PBS solution (Biowest). Tween 20 (Sigma Aldrich) surfactant was added to the solution (0.1%) to avoid microfluidic channel clogging. The solution was mixed on a vortex mixer to disperse particles uniformly.

During the experiments, the Coulter counter and microwave resonator were operated simultaneously. As a particle was passing between the microwave resonator electrodes, it induced an instantaneous shift in capacitance which in turn,

induced phase and amplitude shifts proportional to dielectric permittivity and the size of the particle. While passing between Coulter counter electrodes, the dielectric particle blocked the ionic current between the electrodes, causing a decrease in the current which was measured as a voltage drop through the transimpedance amplifier. Details of the electronic measurement are explained below.

5.4 Electronic Circuit

Similar to previous chapters, resonance frequency and quality factor were measured by VNA before the microparticle sensing experiments. Resonance characteristics depended on the SU8 electrode geometry. The presence of 3D electrodes at the sensing region changes the sensing region capacitance, which in turn affects the resonance characteristics. Among the SU8 electrode designs, designs, the highest signal-to-noise ratio was obtained using the trapezoidal electrodes (width at sensing region : 20µm). Figure 5.2 shows the amplitude response of a split ring resonator with trapezoidal SU8 electrodes. Quality factor was calculated using the 3-dB bandwidth method.

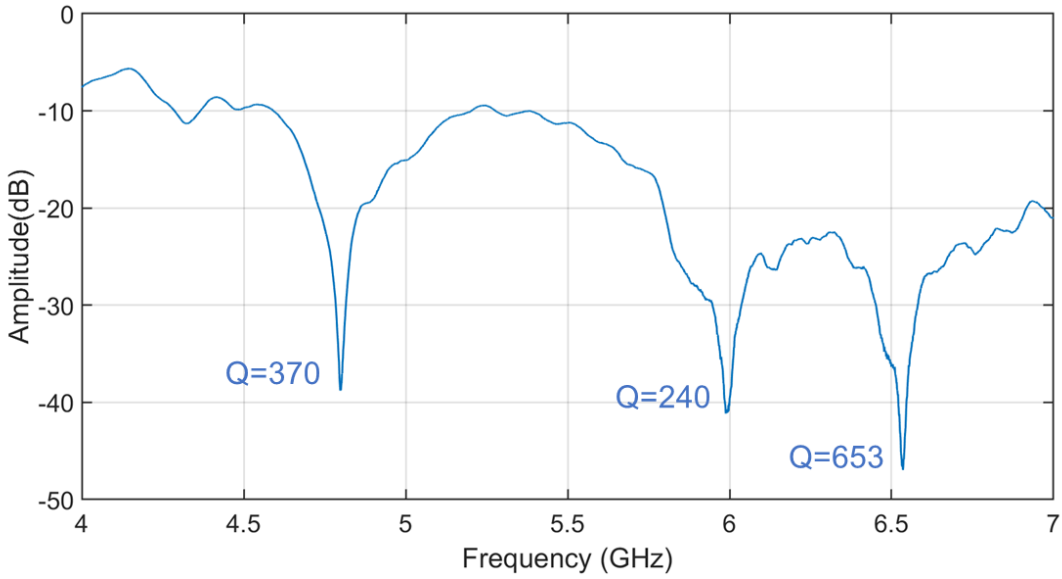

Figure 5.2: Amplitude response of split ring resonator with trapezoidal 3D electrodes

Since the resonance frequency of the split ring resonator was above the operational range of the lock-in amplifier, the same external heterodyne RF circuit as the Chapter 3.3 was used to track the phase and amplitude of the microwave resonator. The resonance frequency was determined through an open loop frequency sweep with the custom-built circuitry after filling the microfluidic channel with PBS . The sensitivity of each prospective resonance frequency was checked by passing several particles back and forth before starting the experiment. The lock-in time constant was changed between the experiments, according to the particle passage time, yet it was usually set to 1 ms to capture particle passage and maximize the signal-to-noise ratio. The data transfer rate was set to 13.4kSa/s.

For the Coulter counter measurements, an external circuit was not required because the highest SNR of the sensor was obtained at around 360kHz which is in the operational regime of the lock-in amplifier. As shown in Figure 5.1, the Coulter counter has 2 electrodes, for excitation and readout. Excitation was directly provided by the lock-in amplifier and, a transimpdance amplifier was used at the readout to convert the current to the voltage. A transimpedance amplifier consists of an operational amplifier and a resistor and its working principle can be explained as follows: No current can leak into the positive input of the amplifier so if negative input is connected to ground, positive input becomes ground as well. When a resistor is connected between the positive input and the output of the operational amplifier, the voltage at the output is proportional to the input current through Ohm's Law. With this setup, the output current of the Coulter counter can be converted into voltage. The electronic circuit used for excitation and readout of the Coulter counter, together with a simple circuitry of transimpedance amplifier is shown in Figure 5.3.

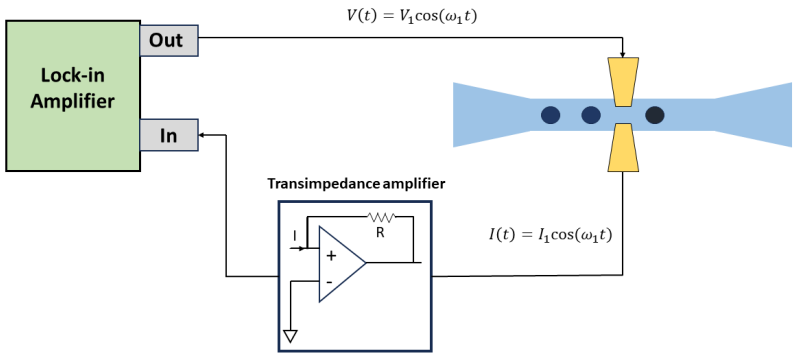

Figure 5.3: Coulter counter electronic circuitry

During the experiments, the lock-in time constant and data transfer rate were set to 1 ms and 14kSa/s, respectively. The internal resistance of the transimpedance amplifier was used as 10kΩ. These parameters were chosen to maximize the signal-to-noise ratio of the Coulter counter. Similar to the microwave resonator, the output amplitude was tracked in an open-loop measurement configuration. The decrease in current induced by a microparticle, rapidly passing between the SU8 electrodes was converted to a voltage drop by the transimpedance amplifier, supplied to the lock-in amplifier and digitally read from the LabOne software.

5.5 Data Analysis

Microwave sensor and Coulter signals were simultaneously analyzed in the custom-built MATLAB script to obtain the size and dielectric permittivity information of a microparticle species (Appendix). The portion of the MATLAB script used for the analysis of the microwave signal was very similar to the codes in Chapters 3 and 4. The initial step of the MATLAB script was resampling microwave and Coulter signals at 10kSa/s because the sampling rates of Coulter and microwave signals were different during the experiments. Baseline reduction was

applied to the signals to compensate for the effect of long-term drift. Data recording in microwave and Coulter signals were manually started, consecutively, and this added a small time delay between the signals. Indices of the same event in Coulter and microwave signals were matched to synchronize the signals. Coulter amplitude signal was normalized by finding the amplitude baseline and dividing the baseline reduced signal by signal baseline.

Microwave amplitude signal was used to determine particle-induced shifts using the *findpeaks* function. The noise level on a blank data set without any events was assigned as a threshold for the peak finder function. Peaks in phase and amplitude signals were matched based on the peak location. Y-quadrature shift was calculated using Equation 3.2. Although the indices of Coulter and microwave signals were matched before, the peaks were still not exactly coincident so the peak locations could not be used for finding the correspondent events. Instead, data points in a certain vicinity of the microwave signal peak location were checked in Coulter and the maximum of these points was assigned as the Coulter amplitude shift. Later, the particle-induced shifts were plotted on the baseline reduced signal.

Finally, the magnitude of the peaks in the Coulter signal (geometrical volume) versus the Y-quadrature shift (electrical volume) was plotted for each particle. In this plot, particles of the same type with different sizes aligned on a line that can be defined as $y{=}mx$ where x is the Coulter signal, geometrical volume, and y is the Y-quadrature shift, electrical volume. For different microparticle species, the slope of the line was different. In the case of monodisperse particles of the same type, particles formed a dense point on the geometrical versus electrical volume scatter plot rather than a line.

The ratio of electrical to geometrical volume was named the opacity and was calculated by dividing the Y-quadrature shift by Coulter signal magnitude. Considering that dY is proportional to the normalized capacitance shift, the ratio of opacity for different microparticles is expected to be proportional to the ratio of their Clausius-Mosotti factor. For an experiment involving different microparticle species, the opacity histogram showed a bimodal distribution. The ratio of

the mean of the peaks was proportional to the ratio of Clausius-Mosotti factor of particles and from Clausius-Mosotti factor, the dielectric permittivity of each microparticle species could be calculated.

5.6 Experiment Results

5.6.1 Polystyrene-Polyethylene Microparticle Experiments

Polystyrene-polyethylene microparticle classification experiments were conducted using the SU8 electrode integrated resonator-Coulter counter sensor architecture. Initially, only polystyrene microparticles between the size range of 14-20 µm were passed through the sensing region. Figure 5.4 shows the geometrical versus electrical volume of 670 polystyrene microparticles.

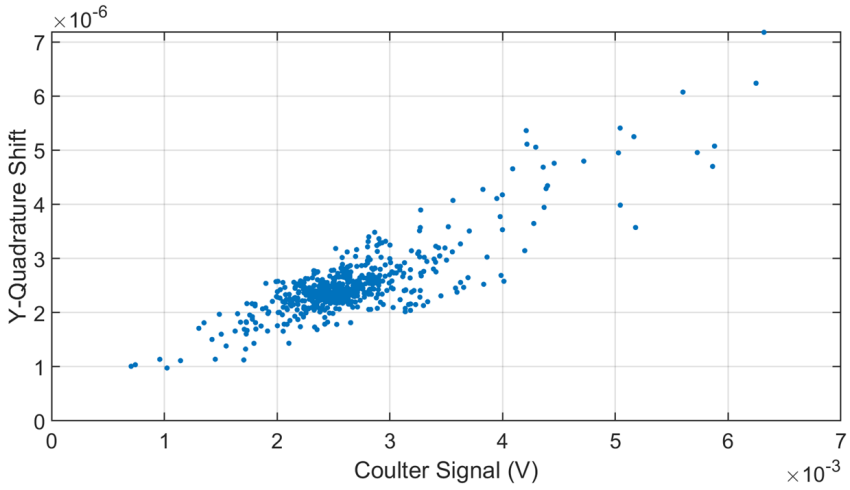

Figure 5.4: Geometrical versus electrical volume of polystyrene microparticles

Geometrical versus electrical volume signals of the particles are aligned on the same line because their dielectric permittivity is the same. On the x-axis, the span of the Coulter signal is proportional to the volume range of the particles inside the solution.

After polystyrene microparticle sensing experiment, polyethylene microparticles were added to the solution and a second experiment was done without changing the experiment parameters. Figure 5.5 shows the geometrical volume versus electrical volume plot for 340 microparticles.

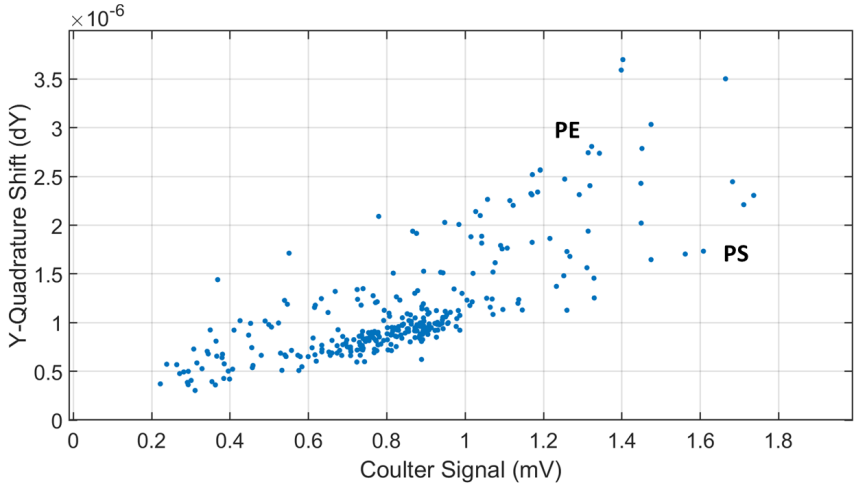

Figure 5.5: Geometrical versus electrical volume of polystyrene and polyethylene microparticles

In comparison to Figure 5.4, the signals from particles are aligned along 2 different lines, corresponding to different microparticle species. The top line is formed by polyethylene and the bottom line is formed by polystyrene microparticles. The size range of polyethylene microparticles is between 10-20 µm and the polystyrene microparticles are between 14-20µm. Accordingly, on the x-axis, the minimum of the polystyrene microparticle Coulter signal is larger than that of the polyethylene. Since the experiments were conducted consecutively, their results were plotted together to check if polystyrene particle signals from the first and second experiments would match each other (Figure 5.6).

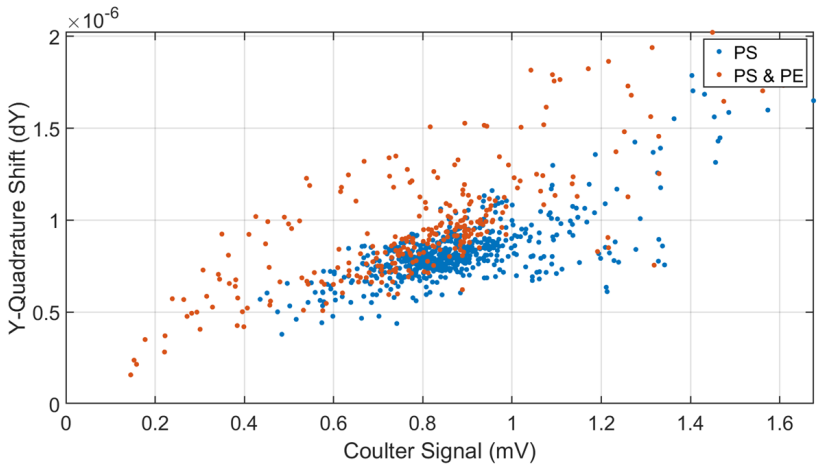

Figure 5.6: Geometrical versus electrical volume for only polystyrene and mixture experiments

Polystyrene microparticle signals from the experiments match each other while the second line corresponding to the polyethylene microparticles appears in the second experiment, indicating that the microparticles could be distinguished from each other. Furthermore, a second experiment was conducted using only polystyrene-polyethylene microparticle mixture to check the repeatability of the above results. Opacity histogram of the second experiment involving 1130 particles is shown in Figure 5.7.

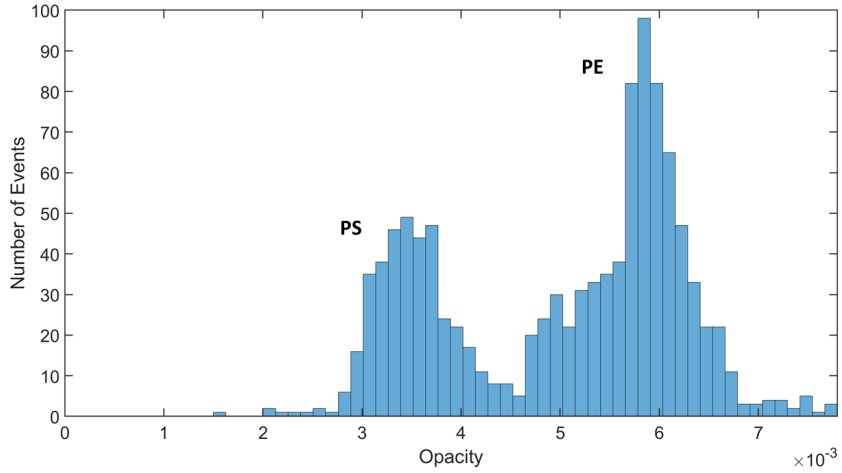

Figure 5.7: Opacity histogram of polystyrene-polyethylene mixture sample

The ratio between the mean of the peaks is expected to be proportional to the Clausius-Mosotti factor of the particles. Theoretically, the Clausius-Mosotti factor of polystyrene and polyethylene are -0.476 and -0.479, respectively and accordingly the ratio between the mean of the peaks should be 1.006. However, on the histogram ratio between the opacity peaks is 1.7. According to data sheet of microparticles, polystyrene microparticle sample is 99.9% pure however polyethylene is around 70% pure, the remaining 30% is classified as proprietary additive [70] [71]. SEM and EDAX analysis were done on the powder samples to check their composition. For the polsytyrene sample, a single carbon peak was observed (Figure 5.8a) while for polyethylene, there was a small titanium peakn The size range and composition of both microparticles were inspected using SEM and EDAX to verify the electrical and geometrical volume signals obtained with the sensor architecture. According to the datasheet, polystyrene microparticles are 99.9% pure and only a carbon peak was observed in EDAX. On the other hand, polyethylene microparticles are 70% the remaining 30% is classified as. Accordingly, the EDAX result of polystyrene shows a single carbon peak (Figure 5.8a) while there is a small titanium peak in polyethylene (Figure 5.8b), causing an increase in the dielectric permittivity. The intensity of the titanium peak is 38 while the intensity of the carbon peak is 1230 in the polyethylene sample yet, the drastic difference between the dielectric permittivities of their materials changes the permittivity of the sample.

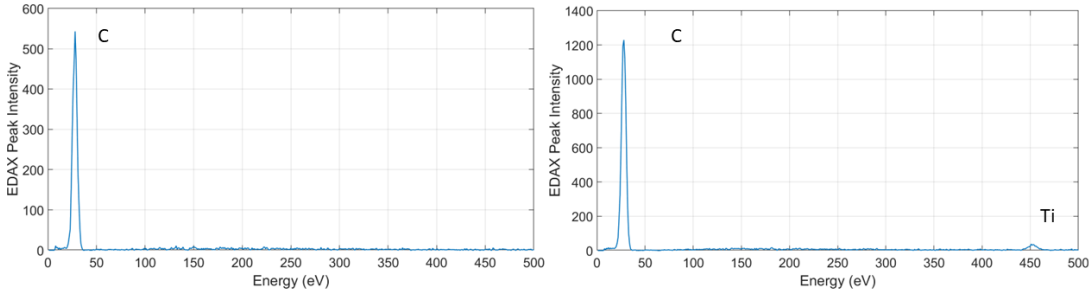

Figure 5.8: EDAX Analysis results of (left) polystyrene (PS) sample (right) polyethylene (PE) sample

EDAX analysis was done using 30kV voltage and 4.0 spot size to penetrate deeper inside the powder sample yet the exact composition and type (core-shell, Janus..) of polyethylene microparticles couldn't be determined completely in EDAX analysis, no further conclusions could be derived about the dielectric permittivity of the sample Theoretically, the dielectric permittivity of both samples, hence their Clausius-Mosotti factor are so close that differentiating the pure samples would be challenging. Yet, due presence of a small amount of titanium dioxide additive inside the polyethylene sample, it was possible to electrically differentiate the microplastic samples.

Chapter 6

Conclusion and Future Perspectives

This thesis presents 2 different methods for the integration of 3D electrodes on microwave resonators to obtain a uniform electric field inside the microfluidic channel and mitigate the position-dependent sensitivity problem. Initially, Galinstan was filled inside dead-end cavities at the sidewalls of the microfluidic channel. Liquid metal access channels were also in contact with the coplanar split ring resonator electrodes at the bottom, this way the electric field between the coplanar electrodes was extended to form a uniform electric field along the microfluidic channel. Using this resonator architecture, 20 and 30µm polystyrene microparticles were differentiated based on their volume, without any height calibration. However, the signal-to-noise ratio (SNR) obtained with this resonator was low to sense cells or particles smaller than 20µm due to the presence of a PDMS spacer between the liquid electrode and the microfluidic channel. Since Galinstan is liquid at room temperature, it was necessary to have a barrier to hinder the metal from leaking into the microfluidic channel. The main design consideration for a future design should be replacing the PDMS spacer between the microfluidic channel and Galinstan electrodes to increase the SNR while avoiding liquid metal leakage.

The second method for the fabrication of the 3D electrodes was pattering SU8 pillars with the same height as the microfluidic channel and metalizing the pillars by sputter deposition. Fabrication of solid 3D electrodes is more complex than liquid electrodes, however, solid electrodes can be placed inside the microfluidic channel to boost the SNR. SU8 microelectrodes were first used in connection with a microstrip transmission line resonator for size-based classification of 12 and 20µm polystyrene microparticles. Particle clusters were differentiated from each other based on the volume without the need for any height compensation algorithm. As mentioned, since 3D electrodes were positioned inside the microfluidic channel SNR increased by 10 times. The ratio of microwave signals induced by 20 and 12µm particles were close to their volumetric ratio, indicating presence of uniform electric field inside the microfluidic channel.

Later, a microwave resonator and Coulter counter, sensors operating at high and low frequencies, were integrated on the same sensor to characterize different microparticle samples such as polystyrene and polyethylene. Dielectric permittivity and size of a microparticle can be measured using microwave since Debye shielding can be overcome at GHz frequencies. On the other hand, Coulter signal only depends on the particle size since the sensor operates at kHz regime. Using both sensors together, microparticles with different permittivity and size regime can be analyzed. This sensor architecture was used to sense and differentiate polystyrene and polyethylene microparticles without any post processing for particle trajectory inside the microfluidic channel. Normally, dielectric permittivity and size range of the particle populations are very close to each other, so differentiating the samples would be challenging. There was titanium additive inside the polyethylene sample, which could be detected by using a microwave resonator and made it possible to differentiate the microplastic samples.

Bibliography

[1] W.R.Hogg and W.H.Coulter, "Apparatus and method for measuring a dividing particle size of a particulate system," US3557352 (1971).

[2] S.Vaidyanathan, H.W.Sachindra, S. T. Gamage, F.Shiri, Z.Zhao, J.Choi, S.Park, M. Witek, C.McKinney, M.Verber, A.R.Hall, K.Childers, T.McNickle, S.Mog, E.Yeh, A.K.Godwin, and S. A. Soper, "High sensitivity extended nano-coulter counter for detection of viral particles and extracellular vesicles,," *Analytical Chemistry*, vol. 95, no. 26, pp. 9892–9900, 2023.

[3] C.G.Brown and J.Clarke, "Nanopore development at oxford nanopore,," *Nature Biotechnology*, vol. 34, pp. 810–811, 2016.

[4] A.Secme, U.Tefek, B.Sarı, H.S.Pisheh, H.D.Uslu, O.A.Calıskan, B.Kucukoglu, R.T.Erdogan, H.Alhmoud, O.Sahin, and M.S.Hanay, "High-resolution dielectric characterization of single cells and microparticles using integrated microfluidic microwave sensors,," *IEEE Sensors*, vol. 23, no. 7, pp. 6517–6529, 2023.

[5] T.Chretiennot, D.Dubuc, and K.Grenier, "A microwave and microfluidic planar resonator for efficient and accurate complex permittivity characterization of aqueous solutions,," *IEEE Transactions on Microwave Theory and Techniques*, vol. 61, no. 2, pp. 972–978, 2013.

[6] M.H.Zarifi, T.Thundat, and M.Daneshmand, "High resolution microwave microstrip resonator for sensing applications,," *Sensors and Actuators A: Physical*, vol. 233, pp. 224–230, 2015.

[7] D. J. Rowen, S. Al-Malki, A. A. Abduljabar, A. Porch, D. A. Barrow, and C. J. Allender, "Improved split-ring resonator for microfluidic sensing,," *IEEE Transactions on Microwave Theory and Techniques*, vol. 62, no. 3, pp. 689–699, 2014.

[8] M. Kelleci, H. Aydogmus, L.Aslanbas, S. Erbil, and M. Hanay, "Towards microwave imaging of cells,," *Lab on a Chip*, vol. 18, pp. 463–472, 2018.

[9] C. Dalmay, M. Cheray, A. Pothier, F. Lalloué, M. Jauberteau, and P. Blondy, "Ultra sensitive biosensor based on impedance spectroscopy at microwave frequencies for cell scale analysis,," *Sensors and Actuators A: Physical*, vol. 162, no. 2, pp. 189–197, 2010.

[10] C.Watts, S.M.Hanham, J.P.K.Armstrong, M.M.Ahmad, M.M.Stevens, and N.Klein, "Microwave dielectric sensing of free-flowing, single, living cells in aqueous suspension,," *IEEE Journal of Electromagnetics, RF and Microwaves in Medicine and Biology*, vol. 4, no. 2, pp. 97–108, 2020.

[11] X.Ma, X.Du, H.Li, X.Cheng, and J. C. M. Hwang, "Ultra-wideband impedance spectroscopy of a live biological cell,," *IEEE Transactions on Microwave Theory and Techniques*, vol. 66, no. 8, pp. 3690–3696, 2018.

[12] J.-C.Chien, A.Ameri, E.-C.Yeh, A. N. Killilea, M.Anwarad, and A. M. Niknejad, "A high-throughput flow cytometry-on-a-cmos platform for single-cell dielectric spectroscopy at microwave frequencies,," *Lab on a Chip*, vol. 18, pp. 2065–2076, 2018.

[13] A.Javed, A. Arif, M.Zubair, M.Q.Mehmood, and K.Riaz, "A low-cost multiple complementary split-ring resonator-based microwave sensor for contactless dielectric characterization of liquids,," *IEEE Sensors*, vol. 20, no. 19, pp. 11326–11334, 2020.

[14] M.N.-Jaric, S.F.Romanuik, G. A. Ferrier, G. E. Bridges, M. Butler, K. Sunley, D. J. Thomson, and M. R. Freeman, "Microwave frequency sensor for detection of biological cells in microfluidic channels,," *Biomicrofluidics*, vol. 12, no. 3, 2009.

[15] A.Secme, H.S.Pisheh, U.Tefek, H. D.Uslu, B.Kucukoglu, Y. Alatas, M.Kelleci, and M. S. Hanay, "On-chip flow rate sensing via membrane deformation and bistability probed by microwave resonators,," *Microfluidics and Nanofluidics*, vol. 27, no. 28, 2023.

[16] U.Tefek, B.Sarı, H.Z.Alhmoud, and M.S.Hanay, "Permittivity-based microparticle classification by the integration of impedance cytometry and microwave resonators,," *Advanced Materials*, vol. 35, no. 46, 2023.

[17] A.D.Ninno, V.Errico, F.R.Bertani, L.Businaro, P.Bisegna, and F.Caselli, "Coplanar electrode microfluidic chip enabling accurate sheathless impedance cytometry,," *Lab on a Chip*, vol. 17, pp. 1158–1166, 2017.

[18] J. Zhong, M.Lianga, and Y. Ai, "Submicron-precision particle characterization in microfluidic impedance cytometry with double differential electrodes,," *Lab on a Chip*, vol. 21, pp. 2869–2880, 2021.

[19] D.Spencer and H.Morgan, "High-speed single-cell dielectric spectroscopy," *ACS Sensors*, vol. 5, no. 2, pp. 423–430, 2020.

[20] J.Zhang, W.Li, M.Li, G.Alici, and N.T.Nguyen, "Particle inertial focusing and its mechanism in a serpentine microchannel,," *Microfluidics and Nanofluidics*, vol. 17, pp. 305–316, 2014.

[21] M.G.Lee, S.Choi, and J.-K.Park, "Three-dimensional hydrodynamic focusing with a single sheath flow in a single-layer microfluidic device,," *Lab on a Chip*, vol. 9, pp. 3155–3160, 2009.

[22] M.Asghari, X. Cao, B.Mateescu, D.v.Leeuwen, M.K.Aslan, S.Stavrakis, and A.J.deMello, "Oscillatory viscoelastic microfluidics for efficient focusing and separation of nanoscale species," *ACS Nano*, vol. 14, no. 1, pp. 422–433, 2020.

[23] J. McGrath, C. Honrado, J. Moore, S. Adair, W. Varhue, A. Salahi, V. Farmehini, B. Goudreau, E. B. S. Nagdas and, T. Bauer, and N. Swami, "Electrophysiology-based stratification of pancreatic tumorigenicity by label-free single-cell impedance cytometry," *Analytica Chimica Acta*, vol. 1101, pp. 90–98, 2020.

[24] Y.-T.Chen and D.Lee, "A bonding technique using hydrophilic su-8," *Journal of Micromechanics and Microengineering*, vol. 17, no. 10, pp. 1978–1984, 2007.

[25] N.Haandbæk, O.With, S. C. Bürgel, F.Heerb, and A. Hierlemann, "Resonance-enhanced microfluidic impedance cytometer for detection of single bacteria," *Lab on a Chip*, vol. 14, no. 17, pp. 3313–3324, 2014.

[26] S.-I. Han and K.-H. Han, "Electrical detection method for circulating tumor cells using graphene nanoplates," *Analytical Chemistry*, vol. 87, no. 20, p. 10585–10592, 2015.

[27] N.Demierre, T.Braschler, P.Linderholm, U.Seger, H. Lintel, and P.Renaud, "Characterization and optimization of liquid electrodes for lateral dielectrophoresis," *Lab on a Chip*, vol. 7, no. 3, pp. 355–365, 2007.

[28] L.Rao, B.Cai, X.-L. Yu, S.-S.Guo, W.Liu, and X.-Z. Zhao, "One-step fabrication of 3d silver paste electrodes into microfluidic devices for enhanced droplet-based cell sorting," *AIP Advances*, vol. 5, no. 5, 2015.

[29] D.McIntyre, A.Lashkaripour, and D.Densmore, "Rapid and inexpensive microfluidic electrode integration with conductive ink," *Lab on a Chip*, vol. 20, no. 20, pp. 3690–3695, 2020.

[30] S.V.Puttaswamy, P.Xue, Y.Kang, and Y.Ai, "Simple and low-cost integration of highly conductive three-dimensional electrodes in microfluidic devices," *Biomed Microdevices*, vol. 17, no. 4, 2015.

[31] A.Sciambi and A.R.Abate, "Generating electric fields in pdms microfluidic devices with salt water electrodes," *Lab on a Chip*, vol. 14, no. 15, pp. 2605–2609, 2014.

[32] W.Tang, D.Tang, Z.Ni, N.Xiang, and H.Yi, "Microfluidic impedance cytometer with inertial focusing and liquid electrodes for high-throughput cell counting and discrimination," *Analytical Chemistry*, vol. 89, no. 5, p. 3154–3161, 2017.

[33] S.G.Yoon and S.T.Chang, "Microfluidic capacitive sensors with ionic liquid electrodes and cnt/pdms nanocomposites for simultaneous sensing of pressure and temperature," *Journal of Materials Chemistry C*, vol. 5, no. 8, pp. 1910–1919, 2017.

[34] M.Sun, P.Agarwal, S.Zhao, Y.Zhao, X.Lu, and X.He, "Continuous on-chip cell separation based on conductivity-induced dielectrophoresis with 3d self-assembled ionic liquid electrodes," *Analytical Chemistry*, vol. 88, no. 16, p. 8264–8271, 2016.

[35] S.Li, M.Li, Y. Hui, W.Cao, W.Li, and W.Wen, "A novel method to construct 3d electrodes at the side wall of microfluidic channel," *Microfluidics and Nanofluidics*, vol. 14, no. 3-4, pp. 499–508, 2013.

[36] H.Guo, X.Lv, W.Chen, Y.Zhong, W.Zou, L.Liu, and H.Yu, "Fabrication of a flexible strain sensor with high-aspect-ratio liquid-metal galinstan," *Advanced Materials Technologies*, vol. 8, no. 1, 2022.

[37] C.Pan, D.Liu, M.J.Ford, and C.Majidi, "Ultrastretchable, wearable triboelectric nanogenerator based on sedimented liquid metal elastomer composite," *Advanced Materials Technologies*, vol. 5, no. 11, 2020.

[38] K.Yamagishi, T.Ching, N.Chian, M.Tan, W.Zhou, S.Y.Huang, and M.Hashimoto, "Flexible and stretchable liquid-metal microfluidic electronics using directly printed 3d microchannel networks," *Advanced Functional Materials*, 2023.

[39] K.Munirathinam, K.Kwon, J.Park, and D.-W.Lee, "Liquid dielectric layer-based microfluidic capacitive sensor for wireless pressure monitoring," *Sensors and Actuators: A.Physical*, vol. 357, 2023.

[40] S.-Y.Tang, J.Zhu, V.Sivan, B.Gol, R.Soffe, W.Zhang, A.Mitchell, and K.Khoshmanesh, "Creation of liquid metal 3d microstructures using dielectrophoresis," *Advanced Functional Materials*, vol. 25, no. 28, pp. 4445–4452, 2015.

[41] B.D.Wiltshire, M. A.Rafi, and M.H.Zarifi, "Microwave resonator array with liquid metal selection for narrow band material sensing," *Scientific Reports*, vol. 11, no. 8598, 2021.

[42] M. A. Rafi, B. D. Wiltshire, and M.H.Zarifi, "Wideband tunable modified split ring resonator structure using liquid metal and 3-d printing,," *IEEE Microwave and Wireless Components Letters*, vol. 30, no. 5, pp. 469–472, 2020.

[43] X.Gao, P.Li, Z.Yang, L.An, Z. Wang, J.Guo, N.Xu, and W.Wang, "Liquid metal-based microfluidic metasurface for controllable electromagnetic wave reflection attenuation," *Journal of the Electron Devices Society*, vol. 10, pp. 898–906, 2022.

[44] S.Zeianli, B.Çetin, S.N.B.Oliaei, and Y.Karpat, "Fabrication of continuous flow microfluidicsdevice with 3d electrode structures for highthroughput dep applications usingmechanical machining," *Electrophoresis*, vol. 36, no. 13, pp. 1432–1442, 2015.

[45] M.T.Güler, I.Bilican, S.Agan, and C.Elbuken, "A simple approach for the fabrication of 3d microelectrodes for impedimetric sensing," *Journal of Micromechanics and Microengineering*, vol. 25, no. 9, 2015.

[46] E.W.Nery, M.K.-Siedlecka, Y.Furuya, and M.J.-Niedziolka, "Pencil lead as a material for microfluidic 3d-electrode assemblies," *Sensors*, vol. 18, no. 11, p. 4037, 2018.

[47] Y.Zhu and P.R.Chiarot, "Directed assembly of nanomaterials using electrospray deposition and substrate-level patterning," *Powder Technology*, vol. 364, pp. 845–850, 2020.

[48] R.T.Erdogan, M.Alkhaled, B.E.Kaynak, H.Alhmoud, H.S.Pisheh, M.Kelleci, I.Karakurt, C.Yanık, Z.B.Sen, B.Sarı, A.M.Yagcı, A.Ozkul, and M.S.Hanay, "Atmospheric pressure mass spectrometry of single viruses and nanoparticles by nanoelectromechanical systems," *ACS Nano*, vol. 16, no. 3, pp. 3821–3833, 2022.

[49] S.H.Lee, G.-Y.Yun, Y.Koh, S.-H.Lee, and Y.-K.Kim, "Fabrication of a 3 dimensional dielectrophoresis electrode by a metal inkjet printing methods," *Micro and Nano Systems Letters*, vol. 1, no. 5, 2013.

[50] X.Min and W.S.Kim, "Artificial xylem chip: A three-dimensionally printed vertical digital microfluidic platform," *Langmuir*, vol. 36, no. 48, p. 14841–14848, 2020.

[51] I.Piekarz, J.Sorocki, M.T.Craton, K.Wincza, S.Gruszczynski, and J.Papapolymerou, "Application of aerosol jet 3-d printing with conductive and nonconductive inks for manufacturing mm-wave circuits," *IEEE Transactions on Components, Packaging and Manufacturing Technology*, vol. 9, no. 3, pp. 586–595, 2019.

[52] L.Wang, L.Flanagan, and A.P.Lee, "Side-wall vertical electrodes for lateral field microfluidic applications," *Journal of Microelectromechanical Systems*, vol. 16, no. 2, pp. 454–461, 2007.

[53] Q.Li and Y.J.Yuan, "Application of vertical electrodes in microfluidic channels for impedance analysis," *Micromachines*, vol. 7, no. 6, 2016.

[54] O.Civelekoglu, R.Liu, N.Asmare, A.K.M.Arifuzzman, and A.F.Sarıoglu, "Wrap-around sensors for electrical detection of particles in microfluidic channels," *Sensors and Actuators B: Chemical*, vol. 375, p. 132874, 2023.

[55] C. et. al., "Bicmos microfluidic sensor for single cell label-free monitoring through microwave intermodulation," *IEEE MTT-S International Microwave Symposium (IMS), IEEE*, pp. 1–4, 2016.

[56] C.Iliescu, G.L.Xu, V.Samper, and F.E.H.Tay, "Fabrication of a dielectrophoretic chip with 3d silicon electrode," *Journal of Micromechanics and Microengineering*, vol. 15, pp. 494–500, 2005.

[57] N. Hu, J. Yang, S. Qian, S. W. Joo, and X. Zheng, "A cell electrofusion microfluidic device integrated with 3d thin-film microelectrode arrays,," *Biomicrofluidics*, vol. 5, no. 3, 2011.

[58] X.Li, J.Duan, Z.Qu, J.Wand, M.Ji, and B.Zhang, "Continuous particle separation driven by 3d ag-pdms electrodes with dielectric electrophoretic force coupled with inertia force,," *Micromachines*, vol. 13, no. 1, p. 117, 2022.

[59] S.Jiguet, A.Bertsch, H.Hofmann, and P.Renaud, "Conductive su8 photoresist for microfabrication,," *Advanced Functional Materials*, vol. 15, no. 9, pp. 1511–1516, 2005.

[60] R.M.-Duarte, P.Renaud, and M.J.Madou, "A novel approach to dielectrophoresis using carbon electrodes,," *Electrophoresis*, vol. 32, no. 17, pp. 2385–2392, 2011.

[61] S.C.Kilchenmann, E.Rollo, P. Maoddi, and C.Guiducci, "Metal-coated su-8 structures for high-density 3-d microelectrode arrays,," *Journal of Microelectromechanical Systems*, vol. 25, no. 3, pp. 425–431, 2016.

[62] P.E.-Thiriet, J.Pezoldt, G.Gambardella, K.Keim, B.Deplancke, and C.Guiducci, "Selective retrieval of individual cells from microfluidic arrays combining dielectrophoretic force and directed hydrodynamic flow,," *Micromachines*, vol. 11, no. 3, p. 322, 2020.

[63] K.Keim, M.Z.Rashed, S.C.Kilchenmann, A.Delattre, A.F.Gonçavles, P.Ery, and C.Guiducci, "On-chip technology for single-cell arraying, electrorotation-based analysis and selective release,," *Electrophoresis*, vol. 40, no. 14, pp. 1830–1838, 2019.

[64] C. PCB, "Microwave resonators." https://resources.pcb.cadence.com/blog/2023-microwave-resonators, 2024. Accessed: 27.04.2024.

[65] G. A. Ferrier, S. F. Romanuik, D. J. Thomson, G. E. Bridges, and M. R.Freeman, "A microwave interferometric system for simultaneous actuation and detection of single biological cells,," *Lab on a Chip*, vol. 9, no. 23, p. 3406, 2009.

[66] B. Küçükoğlu, "Particle sensing with narrowband microwave split ring resonators," 2021.

[67] B. Sarı, "Microparticle classification based on permittivity by the concurrent use of resisitve pulse sensing and microwave resonators," 2022.

[68] A. Seçme, "Bow tie shaped coplanar waveguide microwave resonators for single cell detection, flow rate measurements, and nanopore sensing of viruses," 2020.

[69] B.F.E.Matarèse, P.L.C.Feyen, A.Falco, F.Benfenati, P.Lugli, and J.C.deMello, "Use of su8 as a stable and biocompatible adhesion layer for gold bioelectrodes,," *Scientific Reports*, vol. 5, no. 5560, 2018.

[70] Cospheric Microparticles, *Polystyrene Microspheres, Spheres and Balls Safety Data Sheet*, 2 2024.

[71] Cospheric Microparticles, *Polyethylene Beads, Microspheres and Nanospheres Safety Data Sheet*, 2 2024.

Appendix A

Code

```
%Code for analysis of 3D electrode microwave&coulter
   experiments
%%
% 1-Read LabOne raw data, create time, phase, amplitude
    matrices-also Coulter
S=readtable('meas_plotter_20240531_185527.txt');
S=table2array(S);
L=length(S(:,1));
t=S(1:L/2,1); %time
P=S(1:L/2,2);
A=S(L/2+1:end,2);%microwave
t1=t;

S1=readtable('meas_plotter_20240531_185553.txt');
S1=table2array(S1);
L=length(S1(:,1));
t2=S1(1:L,1); %time
A_CC=S1(1:L,2); %Coulter amplitude

%%
```

```
% 2-Resample data sets
[A,t1] = resample(A,t1,10e3,1,1);
[P,t] = resample(P,t,10e3,1,1);
[A_CC,t2] = resample(A_CC,t2,10e3,1,1);
%%

A=A(65000:2.9e6);
A_CC=A_CC(65000:2.9e6);
P=P(65000:2.9e6);
%%
%3-Baseline removal
WindowSize =12000;
StepSize =12000;
QuantileValue = 0.5;
SmoothMethod = 'none';

x = 1:length(A);
msbackadj(transpose(x),A,'WindowSize',WindowSize,'
   StepSize',StepSize,'QuantileValue',QuantileValue,'
   SmoothMethod',SmoothMethod);
A1= msbackadj(transpose(x),A,'WindowSize',12000,'
   StepSize',12000,'QuantileValue',QuantileValue,'
   SmoothMethod','none');
msbackadj(transpose(x),P,'WindowSize',WindowSize,'
   StepSize',StepSize,'QuantileValue',QuantileValue,'
   SmoothMethod',SmoothMethod);
P1= msbackadj(transpose(x),P,'WindowSize',12000,'
   StepSize',12000,'QuantileValue',QuantileValue,'
   SmoothMethod','none');

x1 = 1:length(A_CC);
```

```
msbackadj(transpose(x1),A_CC,'WindowSize',WindowSize,'
   StepSize',StepSize,'QuantileValue',QuantileValue,'
   SmoothMethod',SmoothMethod);
A1_CC= msbackadj(transpose(x1),A_CC,'WindowSize',12000,
   'StepSize',12000,'QuantileValue',0.5,'SmoothMethod',
   'none');

%%
%4-Match CC and uW signals: We start recording data at
   different
%times-match indices of same events.
matchpar=24000;
A1_CC=A1_CC(matchpar:end);
A_CC=A_CC(matchpar:end);
% A1=A1(18000:end);
% A=A(18000:end);
% P1=P1(18000:end);
% P=P(18000:end);
%%
%5-Normalize Coulter signal
As=A_CC-A1_CC;
An=A1_CC./As;
Ans=An.^2;

%%
%6-Filtering: 2 approaches are possible - FFT & notch
   filter (6.1) or high
%order Savitzky-Golay filter (6.2)
%6.1-FFT
%Check FFT and see where the noise peaks are
fsample=10000; %Hz
a=fftshift(fft(A1-mean(A1)));
```

```
f=linspace(-fsample/2,fsample/2,length(a));

loglog(f,abs(a)/length(a))
hold on
%%
%Apply notch filter for the specific frequencies on FFT
[num1,den1] = iirnotch(50/(fsample/2),2/(fsample/2));

g1=filtfilt(num1,den1,A1);

p1=filtfilt(num1,den1,P1);

[num1,den1] = iirnotch(100/(fsample/2),4/(fsample/2));

g2=filtfilt(num1,den1,A1);
p2=filtfilt(num1,den1,P1);

figure(1)
plot(A1,'k','LineWidth',1);
hold on
plot(g2,'r','LineWidth',1)


figure(2)
plot(P1,'k','LineWidth',1);
hold on
plot(p2,'r','LineWidth',1)

%%
%6.2 High order Savitzky-Golay Filter
%Savitzky-Golay can be used for reducing noise in data
   sets with peaks.
```

```
%We use a very high order filter so that it encompasses
    the noise in the
%signal (filtered data is similar to the level of noise
   ). Through
%subtracting the filtered data from actual signal we
   get straight baseline.
%Filter parameters are arbitrarily selected.

% a1=sgolayfilt(A1,11,9901);
% p1=sgolayfilt(P1,11,9901);
% acc1=sgolayfilt(A1_CC,11,9901);
an=sgolayfilt(An,15,9011);
%
% A2=A1-a1;
% P2=P1-p1;
% A2_CC=A1_CC-acc1;
An1=An-an;
%%
%6.3 Take square-square root
P1=-P1;
for i = 1:length(A1)
    if A1(i)<0
      A1(i)=0;
      P1(i)=0;
    end
end
%%
P1s=P1.^2;
A1s=A1.^2;
%%
%6-Find peaks
```

```
[pks5,locs5,width5,prominence5]=findpeaks(-P1,'
   MinPeakProminence',1.5E-4,'MinPeakDistance',500);
% pks3=sqrt(pks3);

%%
sel_PSS =selected;
PSS_index = [];
L_PSS=length(sel_PSS(:,1));
for j = 1:L_PSS
    b = find(pks3==sel_PSS(j,2));
    b = b(1);
    PSS_index = [PSS_index b];
end
%%
%7-Calculate microwave baseline, find raw phase and
   amplitude and phase
%shifts on microwave data using peak locations
A_br1=A-A1;
P_br1=P-P1;
dP5=-A1(locs5);
% dP3=sqrt(dP3);

Ar5=P_br1(locs5);
Pr5=A_br1(locs5);
%%
% for i =1:length(locs3)
%     int{i}=-P1(locs3(i)-750:locs3(i)+750);
%     dP3(i)=max(int{i});
% end

%Visualization of peaks
% figure(1)
% plot(A1)
```

```
% hold on
% plot(locs1,pks1,'.')
%
% figure(2)
% plot(P1)
% hold on
% plot(locs1,dP1,'.')

%%
% %8-Find the Coulter signal corresponding to each data
    point
% for i =1:length(locs3(PSS_index))
%     int{i}=An1(locs3(PSS_index(i))-1000:locs3(
   PSS_index(i))+1000);
%     dRcc3p(i)=max(int{i});
% end
for i =1:length(locs5)
    int{i}=-An(locs5(i)-1000:locs5(i)+1000);
    dRcc5n(i)=max(int{i});
end
% dRcc3n=sqrt(dRcc3n);
% %
% dRcc3=dRcc3n+dRcc3p;
% % figure(3)
% plot(Ans)
% hold on
% plot(locs3,dRcc3n.^2,'.')
%%
%9-Calculate dY and hidden phase
for i =14:20
    %phi(i)=3.665+0.209*i;%finer
    phi(i)=(pi/3)+i*(pi/12);
%     phi(i)=1.2+i*0.508;%coarse
```

```
%     dY3 = pks3.*sin(Pr3.*(pi/180)+phi(i)) + Ar3.*cos(
   Pr3.*(pi/180)+phi(i)).*-dP3.*(pi/180);
dY5 =-pks5.*sin(Pr5.*(pi/180)+phi(i)) + Ar5.*cos(Pr5.*(
   pi/180)+phi(i)).*-dP5.*(pi/180);

    h1=histogram(dY5,20);

    hold on

% %
% plot(dY1.^1/3,'.')
%     hold on
    legend('1','2','3','4','5')
end
%
%%
%10-Opacity&plots
dY5=-pks5.*sin(Pr5.*(pi/180)+5.105) + Ar5.*cos(Pr5.*(pi
   /180)+5.105).*-dP5.*(pi/180);

%%

% % % % figure(5)
% dY3 = dY3(1:265);
% dY2=abs(dY2);
% dRcc3=dRcc3';
scatter(dRcc5n.^1/3,dY5.^1/3,'filled')
```